공학박사 학위논문

Design of Charge Transporting Layers for Organic-Inorganic Hybrid Perovskite Solar Cells

유무기 하이브리드 페로브스카이트 태양전지의 전하이동층 연구

2020년 2월

서울대학교 대학원

재료공학부

박 민 아

Abstract

Design of Charge Transporting Layers for Organic-Inorganic Hybrid Perovskite Solar Cells

Min-Ah Park
Department of Materials Science and Engineering
The Graduate School
Seoul National University

Organic-inorganic hybrid perovskite materials have significant properties such as high absorption coefficient, long carrier diffusion length, low exciton binding energy, and tunable band gap. Owing to these advantages, organic-inorganic hybrid perovskite materials have attracted considerable attention in photo-electronics field such as solar cells, light emitting diodes, and photodetectors. In particular, solar cells based on organic-inorganic hybrid materials have shown enormous developments in a short time since 2009, rapidly reaching high photoconversion efficiencies over 25%. However, organic-inorganic hybrid perovskite solar cells have issues on the stability, rigidity, and transparency, which limit the commercialization of perovskite solar cells. In this thesis,

the strategies were proposed to address the issue, and the possibility of commercialization was demonstrated through translucent perovskite solar cell structures.

First, a Li-doped NiO_x hole-extraction layer that shows significantly improved fill factor compared with the pure NiO_x counterpart was demonstrated. It is also found that the annealing temperature for the NiO_x layer can be lowered by doping Li ions. However, the Li doping does not influence the photocurrent and photovoltage, leading to the increased conversion efficiency. The conductive atomic force microscope study reveals that the addition of Li ions to NiO_x significantly increases the conductivity of the NiO_x layer, and thus decreases the series resistance of the device, resulting in the increased fill factor and conversion efficiency.

Second, the GO layer with the appropriate thickness can exhibit high transmittance, extract holes efficiently from the perovskite layer, and block water/oxygen permeation from the substrate, indicating that GO can be used as a good HTM of the perovskite solar cells. In particular, the barrier properties of the GO layer successfully compensate the relatively high water/oxygen permeability of the polyethylene naphthalate (PEN) substrates, and significantly improve the long-term stability of the flexible perovskite solar cells. In addition, transparent perovskite solar cells are prepared by replacing the conventional Ag top electrode with the indium tin oxide (ITO) top electrode, enabling the bi-facial light illumination, thereby allowing various new optoelectronic applications of perovskite materials such as high-efficiency tandem solar cells, building-integrated photovoltaics (BIPVs), and displays.

Third, the Spiro-OMeTAD/WO_3 double layer enable the perovskite solar cell to have the transparent electrodes on the both sides. The WO_3 film protects underlying

layers from sputtering damage caused by ITO deposition process and plays a role as hole transporting layer with Spiro-OMeTAD. The perovskite solar cell with transparent electrodes on the both sides exhibits device characteristics comparable to the solar cell with opaque Au electrode. The introduction of WO_3 film through a solution and low temperature method allow the perovskite solar cell to facilitate the application to various devices such as BIPVs, bi-facial solar modules, and the tandem solar cells.

This thesis focused on the solutions to current issues of perovskite solar cells such as lack of stable charge transporting materials, rigid device structure, and opaque electrode. The results including the stable inorganic or carbon-based hole transporting materials, flexibility of device, and transparent structure are expected to propose the possibility to solve the issues of perovskite solar cells and to demonstrate the feasibility of commercialization.

Keywords: Perovskite solar cell, Charge transporting layer, Hole transporting layer, Bi-functional layer, Buffer layer, Low temperature process, Long-term stability, Transparent electrode

Student Number: 2017-33377

Table of Contents

List of Tables

List of Figures

Chapter 1. Introduction

1.1 Solar energy as Renewable energy

Energy consumption in various forms have been increasing rapidly with the development of society and industry. This causes depletion of fossil fuels and environmental pollution, which is a problem to be solved. Therefore, efforts have been made to develop eco-friendly energy around the world. Among eco-friendly energies, the amount of solar energy reaching the surface of the planet is so huge that it is about twice the amount that can be obtained from all non-renewable resources of the earth in one year.[1.1] Various technology have been studied to convert such enormous amounts of solar energy into necessary energy forms such as photovoltaic (PV), solar heating and cooling. In particular, photovoltaic power generation has been studied in various sizes, from large modules to small elements, and can be used in a wide range of applications. However, even the most commonly used silicon-based solar cells cost $ 0.6 / W, making them less economical than existing energy sources. Therefore, the ultimate goal of current solar cell research is to lower the cost of power generation and then replace fossil and nuclear energy. Grid parity (the point at which solar power generation costs become the same as existing power generation costs) is expected to be achieved by 2020 in the Republic of Korea, but the problem is that it is not easy to lower the cost of silicon solar cells. Therefore, research of next generation solar cell is needed.

1.2 Perovskite solar cells

Recently, organic and inorganic perovskite solar cells have attracted attention as next-generation solar cells that can solve the cost problem of silicon solar cells. Perovskite solar cells use an organic-inorganic composite material with a perovskite structure as a light absorber. The solar cell has most of the properties required for next-generation solar cells, including the advantages of high efficiency, low materials and manufacturing costs, and facile manufacturing methods. Perovskite solar cells first appeared in 2009,[1.2] and developments have been made by applying perovskite materials to dye-sensitized solar cells and organic solar cell structures. Currently, the highest energy conversion efficiency has been improved to a level similar to that of silicon solar cells, recording more than 25% as shown in Figure 1.1.[1.3]

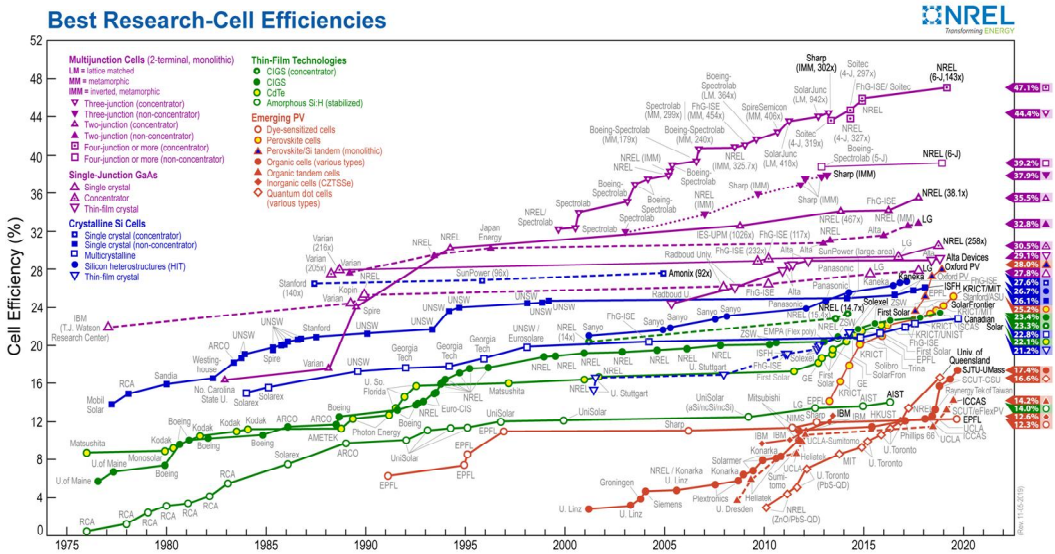

Figure 1.1 The latest chart on record solar cell efficiencies

1.3 Current issues on perovskite solar cells

Although much research has been conducted for a dramatic increase in perovskite solar cell efficiency, many problems remain for commercialization and application to various devices. First, it is important to ensure the stability of the perovskite solar cells.[1.4, 1.5] Many studies were conducted to replace methyl ammonium ion with inorganic ion such as Ru and Cs, which enhanced the stability of the solar cells.[1.6-1.11] The hole transporting layer, electron transporting layer, and electrodes that make up solar cells have also been researched as factors to improve stability. In addition, the encapsulation technology protects the solar cells from the external environment.[1.12, 1.13]

Flexibility studies have also been conducted for use in various applications and environments of perovskite solar cells. In some studies, glass substrates were replaced with PEN, PET, etc., resulting in flexible perovskite solar cells.[1.14-1.16] Commonly used titanium oxides have been replaced with polymeric materials or doped with metal elements for low temperature processes.

In addition, research has begun to replace opaque metal electrodes with transparent conductive electrodes to ensure device transparency.[1.17, 1.18] By using a perovskite solar cell with transparent electrodes on both sides, the color of the light absorbing material can be displayed as it is. Also, high-efficiency solar cells can be manufactured via tandem elements with other solar cells and can be used in various

applications such as displays and building integrated photovoltaics (BIPVs).

1.4 Aim and Strategies

Organic-inorganic hybrid solar cells are attracting attention as next-generation solar cells that are commercially available based on the rapid increase in photoelectric conversion efficiency. While research on organic-inorganic hybrid perovskite materials has been mainly focused, studies on charge transfer layers should be carried out simultaneously for commercialization of solar cells and application to various devices. Therefore, the objective of this thesis is to optimize the electrical and optical properties of charge transporting materials and study the effects on the performance and stability of solar cells through experimental verification.

In chapter 2, the perovskite solar cell is introduced. The structure and classification of the solar cell were described, including light absorbing layer, the perovskite material, the hole transporting material, and the electron transporting material.

In chapter 3, the materials used for the study and the experimental methods are described. The details include the fabrication of solar cells, the method for synthesizing and depositing perovskite, the hole transporting layer, and electron transporting layer. In addition, analytical methods that performs solar cell characteristics and device evaluation were presented.

In chapter 4, the nickel oxide was studied as hole transporting layer This study presented the possibility of overcoming the device stability limitations of existing organic based materials. In addition, the quantitative correlation between the electrical properties of the Li-doped nickel oxide and the device performance was investigated. An

inorganic oxide was also deposited on the electron transport layer, and a transparent conductive oxide electrode was deposited on the top to realize a perovskite solar cell having a p-i-n structure capable of bidirectional illumination.

In chapter 5, perovskite solar cell was studied utilizing graphene oxide as hole transporting layer. The perovskite solar cell using graphene as the hole transporting layer improved the optical conversion efficiency by controlling the optical characteristics of the electrically uniformly deposited graphene oxide charge transfer layer. The performance and stability evaluation of the device verified that the graphene oxide charge transfer layer had a gas barrier effect in the flexible device and emphasized its versatility. Finally, flexibility and long-term stability were ensured for the p-i-n structure solar cells capable of bi-facial illumination.

In chapter 6, the spiro-OMeTAD/WO_3 hole transporting double layer was introduced to form a protective layer for the deposition of transparent conductive oxide electrode of n-i-p structure perovskite solar cells. Through the analysis of the thin film structure of the WO3 layer and the electrical characteristics of the device, the correlation between the protection layer and the device performance was identified and optimized. In addition, the reliability of the correlation was verified by analyzing the electrical and optical characteristics of the organic / inorganic bilayer depending on the presence and absence of the inorganic layer.

1.5 Bibliography

[1.1] "Exergy Flow Charts – GCEP". stanford.edu. http://gcep.stanford.edu/research/exergycharts.html.

[1.2] A. Kojima, K. Teshima, Y. Shirai and T. Miyasaka, Journal of the American Chemical Society, 2009, 131, 6050-6051.

[1.3] Best Research-Cell Efficiency Chart. https://www.nrel.gov/pv/cell-efficiency.html.

[1.4] A. Mei, X. Li, L. Liu, Z. Ku, T. Liu, Y. Rong, M. Xu, M. Hu, J. Chen, Y. Yang, M. Grätzel and H. Han, Science, 2014, 345, 295-298.

[1.5] I. C. Smith, E. T. Hoke, D. Solis-Ibarra, M. D. McGehee and H. I. Karunadasa, Angewandte Chemie International Edition, 2014, 53, 11232-11235.

[1.6] J. Troughton, N. Gasparini and D. Baran, Journal of Materials Chemistry A, 2018, 6, 21913-21917.

[1.7] L. A. Frolova, Q. Chang, S. Y. Luchkin, D. Zhao, A. F. Akbulatov, N. N. Dremova, A. V. Ivanov, E. E. M. Chia, K. J. Stevenson and P. A. Troshin, Journal of Materials Chemistry C, 2019, 7, 5314-5323.

[1.8] U. Khan, Y. Zhinong, A. A. Khan, A. Zulfiqar and N. Ullah, Nanoscale Research Letters, 2019, 14, 116.

[1.9] M. Zhang, J. S. Yun, Q. Ma, J. Zheng, C. F. J. Lau, X. Deng, J. Kim, D. Kim, J. Seidel, M. A. Green, S. Huang and A. W. Y. Ho-Baillie, ACS Energy Letters, 2017, 2, 438-444.

[1.10] Y.-K. Jung, J.-H. Lee, A. Walsh and A. Soon, Chemistry of Materials, 2017, 29, 3181-3188.

[1.11] I. J. Park, M. A. Park, D. H. Kim, G. D. Park, B. J. Kim, H. J. Son, M. J. Ko, D.-K. Lee, T. Park, H. Shin, N.-G. Park, H. S. Jung and J. Y. Kim, The Journal of Physical Chemistry C, 2015, 119, 27285-27290.

[1.12] Y. Han, S. Meyer, Y. Dkhissi, K. Weber, J. M. Pringle, U. Bach, L. Spiccia and Y.-B. Cheng, Journal of Materials Chemistry A, 2015, 3, 8139-8147.

[1.13] H. C. Weerasinghe, Y. Dkhissi, A. D. Scully, R. A. Caruso and Y.-B. Cheng, Nano Energy, 2015, 18, 118-125.

[1.14] K. Li, J. Xiao, X. Yu, T. Li, D. Xiao, J. He, P. Zhou, Y. Zhang, W. Li, Z. Ku, J. Zhong, F. Huang, Y. Peng and Y. Cheng, Scientific Reports, 2018, 8, 442.

[1.15] S. Pisoni, F. Fu, T. Feurer, M. Makha, B. Bissig, S. Nishiwaki, A. N. Tiwari and S. Buecheler, Journal of Materials Chemistry A, 2017, 5, 13639-13647.

[1.16] L. Hou, Y. Wang, X. Liu, J. Wang, L. Wang, X. Li, G. Fu and S. Yang, Journal of Materials Chemistry C, 2018, 6, 8770-8777.

[1.17] F. Fu, T. Feurer, T. Jäger, E. Avancini, B. Bissig, S. Yoon, S. Buecheler and A.

N. Tiwari, Nature Communications, 2015, 6, 8932.

[1.18] X. Wang, Z. Li, W. Xu, S. A. Kulkarni, S. K. Batabyal, S. Zhang, A. Cao and L. H. Wong, Nano Energy, 2015, 11, 728-735.

Chapter 2. Background and Literature Survey

2.1 Perovskite Solar Cell

2.1.1 Perovskite Materials

The perovskite comes from the calcium mineral oxide ($CaTiO_3$), a mineral found in the Urals of Russia in 1839, named after the Russian mineralogist Lev Perovski (1792-1856).[2.1] The term perovskite is used to refer to a material whose crystal structure is the same as that of $CaTiO_3$. In general, it has the structure of ABX_3, where A and B are cations, and X is an anion bound to them. Most of the perovskite materials studied to date have been mainly ABO_3 oxides, such as $CaTiO_3$, $BaTiO_3$, $MgSiO_3$, and $SrZrO_3$. This material exhibits a wide range of conductivity from insulating properties to semiconductors and superconductors depending on the composition. Recently, perovskite materials have been spotlighted as materials for solar cells, and this perovskite has a three-dimensional structure and is composed of the A site of organic cations ($CH_3NH_3^+$, $HC(NH_2)_2^+$),[2.2-2.4] the B site of metal cations (Pb^{2+}, Sn^{2+}),[2.5-2.7] and the X site of halogen anions (I^-, Br^-, Cl^-).[2.8-2.11] (Figure 2.1)

2.1.2 Operation Principle

The perovskite layer absorbs light with energy above the perovskite band gap and forms electron-hole pairs. It is dissociated into electrons and holes, respectively,

electrons go out to ETL, holes go out to HTL, and move to each electrode to produce a current.[2.12] (Figure 2.2)

2.1.3 Classification

Mesoscopic vs. Planar structure Perovskite solar cells are classified into a mesoscopic structure and a planar structure based on the structure of the charge transfer layer. Mesoscopic structures include charge transfer layers that are mesoporous in structures obtained from previous dye-sensitized solar cells. On the other hand, the perovskite exhibits a long carrier diffusion length from hundreds of nanometers to hundreds of micrometers, so that a planar structure can be formed without a mesoporous n-type semiconductor by light-absorbing layer of sufficient thickness.[2.13] (Figure 2.3)

n-i-p vs. p-i-n The structure of the device may be divided according to the direction in which electrons and holes are extracted. In n-i-p structure, the electrons are extracted to the TCO electrode and the holes are extracted to the metal electrode. On the contrary, the structure in which holes are extracted to the TCO electrode and electrons to the metal electrode is called p-i-n structure or inverted structure. This classification can be given in order of manufacturing solar cells. Currently, the highest efficiency solar cell is implemented through the n-i-p structure, but the p-i-n structure shows less hysteresis and is easy to make a tandem device with a Si solar cell.[2.13-2.17] (Figure 2.3)

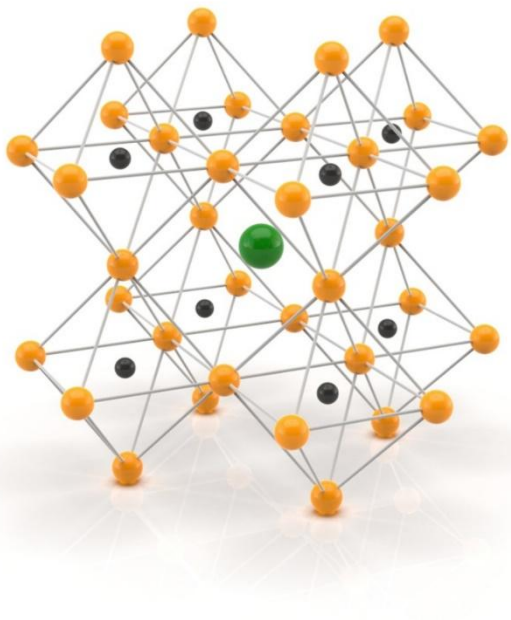

Figure 2.1 Organic-inorganic hybrid perovskite structure

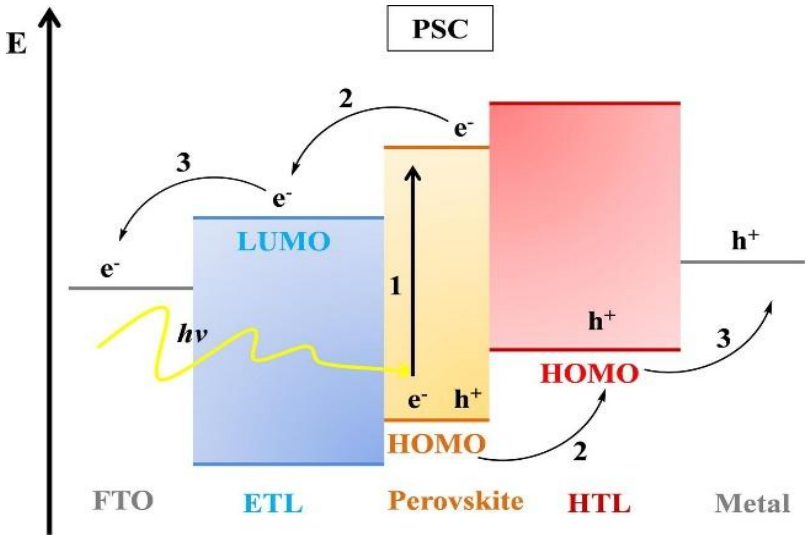

Figure 2.2 Schematic diagram of solar cell operation[2.12]

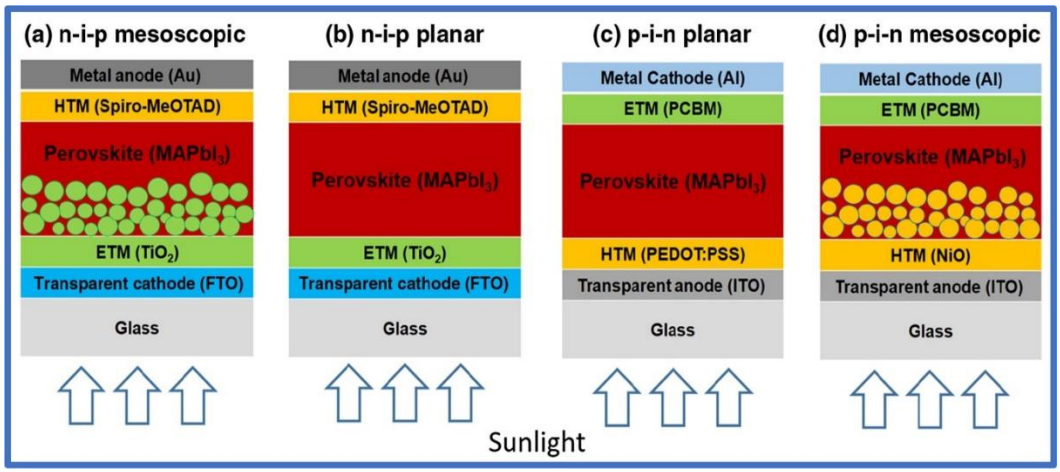

Figure 2.3 Classification of perovskite solar cells[2.13]

2.2 Charge Transporting Materials

2.2.1 Hole Transporting Materials

The hole transporting layer (HTL), which plays a role in transporting holes generated in the perovskite layer, should have a valence band maximum (VBM) higher than that of the perovskite. In the p-i-n structure, since light reaches the perovskite layer through the HTL, it must have a large bandgap energy so as not to interfere with the absorption of light. Also, there should be no reactivity with the perovskite layer because it directly contacts with the perovskite layer. NiO, PEDOT: PSS, CuSCN, CuI, etc. are used in the p-i-n structure,[2.18-2.21] and spiro-OMeTAD, PTAA, etc. are used in the n-i-p structure.[2.22, 2.23] In the early stages of research, the focus was on improving the efficiency, but recently, research has been conducted to satisfy more conditions such as application to the flexible solar cell and improvement of stability as well as the high efficiency.

2.2.2 Electron Transporting Materials

The electron transporting material has a lower conduction band minimum (CBM) than that of the perovskite material and is required excellent charge transfer properties for smooth transfer of electrons generated in the perovskite material. In the n-i-p structure, the band gap energy of ETL must be large so as not to affect the light absorption of the perovskite layer. TiO_2 and ZnO are mainly used in the n-i-p structure

solar cells.[2.24-2.26] In the study using the p-i-n structure, PCBM was deposited by a solution process using a nonpolar solvent that does not dissolve perovskite material, or C_{60} was deposited by thermal evaporation.[2.27, 2.28] In recent years, research on the development of characteristics of ETM has shown that the electron collecting efficiency is increased to increase the photoelectric conversion efficiency of the solar cell device, and it has been found to be a factor to increase the reliability of the device by reducing the hysteresis when measuring the device.[2.29, 2.30]

2.3 Bibliography

[2.1] Minerals: Their Constitution and Origin, Cambridge University Press, 2004.

[2.2] N. J. Jeon, J. H. Noh, W. S. Yang, Y. C. Kim, S. Ryu, J. Seo and S. I. Seok, Nature, 2015, 517, 476-480.

[2.3] S.-H. Turren-Cruz, A. Hagfeldt and M. Saliba, Science, 2018, 362, 449-453.

[2.4] M. Wang, X. Jiang, J. Bian, Y. Feng, C. Wang, Y. Huang, Y. Zhang and Y. Shi, ACS Applied Materials & Interfaces, 2019, 11, 2989-2996.

[2.5] W. Ke and M. G. Kanatzidis, Nature Communications, 2019, 10, 965.

[2.6] C. Liu, J. Fan, H. Li, C. Zhang and Y. Mai, Scientific Reports, 2016, 6, 35705.

[2.7] S. Shao, J. Liu, G. Portale, H.-H. Fang, G. R. Blake, G. H. ten Brink, L. J. A. Koster and M. A. Loi, Advanced Energy Materials, 2018, 8, 1702019.

[2.8] D. W. de Quilettes, S. M. Vorpahl, S. D. Stranks, H. Nagaoka, G. E. Eperon, M. E. Ziffer, H. J. Snaith and D. S. Ginger, Science, 2015, 348, 683-686.

[2.9] E. Edri, S. Kirmayer, S. Mukhopadhyay, K. Gartsman, G. Hodes and D. Cahen, Nature Communications, 2014, 5, 3461.

[2.10] B. Suarez, V. Gonzalez-Pedro, T. S. Ripolles, R. S. Sanchez, L. Otero and I. Mora-Sero, The Journal of Physical Chemistry Letters, 2014, 5, 1628-1635.

[2.11] Y. Tu, J. Wu, Z. Lan, X. He, J. Dong, J. Jia, P. Guo, J. Lin, M. Huang and Y. Huang, Scientific Reports, 2017, 7, 44603.

[2.12] N. Marinova, S. Valero and J. L. Delgado, Journal of Colloid and Interface Science, 2017, 488, 373-389.

[2.13] Z. Song, S. Watthage, A. Phillips and M. Heben, Journal of Photonics for Energy, 2016, 6, 022001.

[2.14] K. A. Bush, A. F. Palmstrom, Z. J. Yu, M. Boccard, R. Cheacharoen, J. P. Mailoa, D. P. McMeekin, R. L. Z. Hoye, C. D. Bailie, T. Leijtens, I. M. Peters, M. C. Minichetti, N. Rolston, R. Prasanna, S. Sofia, D. Harwood, W. Ma, F. Moghadam, H. J. Snaith, T. Buonassisi, Z. C. Holman, S. F. Bent and M. D. McGehee, Nature Energy, 2017, 2, 17009.

[2.15] G. E. Eperon, T. Leijtens, K. A. Bush, R. Prasanna, T. Green, J. T.-W. Wang, D. P. McMeekin, G. Volonakis, R. L. Milot, R. May, A. Palmstrom, D. J. Slotcavage, R. A. Belisle, J. B. Patel, E. S. Parrott, R. J. Sutton, W. Ma, F. Moghadam, B. Conings, A. Babayigit, H.-G. Boyen, S. Bent, F. Giustino, L. M. Herz, M. B. Johnston, M. D. McGehee and H. J. Snaith, Science, 2016, 354, 861-865.

[2.16] J. H. Heo, H. J. Han, D. Kim, T. K. Ahn and S. H. Im, Energy & Environmental Science, 2015, 8, 1602-1608.

[2.17] H.-B. Kim, H. Choi, J. Jeong, S. Kim, B. Walker, S. Song and J. Y. Kim,

Nanoscale, 2014, 6, 6679-6683.

[2.18] H. Wang, Z. Yu, J. Lai, X. Song, X. Yang, A. Hagfeldt and L. Sun, Journal of Materials Chemistry A, 2018, 6, 21435-21444.

[2.19] N. Arora, M. I. Dar, A. Hinderhofer, N. Pellet, F. Schreiber, S. M. Zakeeruddin and M. Grätzel, Science, 2017, 358, 768-771.

[2.20] X. Xu, Z. Liu, Z. Zuo, M. Zhang, Z. Zhao, Y. Shen, H. Zhou, Q. Chen, Y. Yang and M. Wang, Nano Letters, 2015, 15, 2402-2408.

[2.21] L. Hu, M. Li, K. Yang, Z. Xiong, B. Yang, M. Wang, X. Tang, Z. Zang, X. Liu, B. Li, Z. Xiao, S. Lu, H. Gong, J. Ouyang and K. Sun, Journal of Materials Chemistry A, 2018, 6, 16583-16589.

[2.22] G.-W. Kim, G. Kang, J. Kim, G.-Y. Lee, H. I. Kim, L. Pyeon, J. Lee and T. Park, Energy & Environmental Science, 2016, 9, 2326-2333.

[2.23] Z. Hawash, L. K. Ono and Y. Qi, Advanced Materials Interfaces, 2018, 5, 1700623.

[2.24] Z. Guo, L. Gao, C. Zhang, Z. Xu and T. Ma, Journal of Materials Chemistry A, 2018, 6, 4572-4589.

[2.25] M. H. Kumar, N. Yantara, S. Dharani, M. Graetzel, S. Mhaisalkar, P. P. Boix and N. Mathews, Chemical Communications, 2013, 49, 11089-11091.

[2.26] D.-Y. Son, J.-H. Im, H.-S. Kim and N.-G. Park, The Journal of Physical

Chemistry C, 2014, 118, 16567-16573.

[2.27] J. Seo, S. Park, Y. Chan Kim, N. J. Jeon, J. H. Noh, S. C. Yoon and S. I. Seok, Energy & Environmental Science, 2014, 7, 2642-2646.

[2.28] G. Namkoong, A. A. Mamun and T. T. Ava, Organic Electronics, 2018, 56, 163-169.

[2.29] F. Ali, N. D. Pham, L. Fan, V. Tiong, K. Ostrikov, J. M. Bell, H. Wang and T. Tesfamichael, ACS Applied Energy Materials, 2019, 2, 5456-5464.

[2.30] B. Zhao, G. Niu, Q. Dong, J. Liu, N. Li, J. Li and L. Wang, Journal of Materials Chemistry A, 2018, 6, 23797-23804.

Chapter 3. Experiments

3.1 Preparation of Charge Transporting Layers

3.1.1 Li-doped NiOx films

A nickel oxide solution containing 0.1 M nickel (II) acetate tetrahydrate (Sigma-Aldrich, > 99.0% purity) and ethanol was dispersed by sonication. Nickel oxide films were prepared by spin-coating at 1000 rpm 0.1 M nickel (II) acetate tetrahydrate solution on ITO-coated glass substrates, followed by drying for 10min and annealing at 200 C for 1hr. In case of Li-doped nickel oxide film, the concentrations of Li in the precursor solution were adjusted by mixing lithium acetate dehydrate (Sigma-Aldrich, 99.999%) to form 2, 5, 10, and 15% Li-added solutions

3.1.2 Graphene Oxide Films

GO was synthesized according to the modified Hummer's method.[3.1, 3.2] Graphite (6 g) was pre-oxidized for 24 h with potassium persulfate (12 g) and phosphorus pentoxide (12 g) dissolved in sulfuric acid (60 mL) at 80°C. Pre-oxidized graphite was filtrated and rinsed with plenty amount of DI water. After kept under room temperature in vacuum oven, dried expanded graphite (2 g) was dispersed in H_2SO_4. Dispersed solution was stored at 0°C and was stirred at 35°C with 250 rpm for 2 h when it was reacted $KMnO_4$ (12 g). Then, excess amount of ice and H_2O_2 (10 mL) was added

to the solution. This mixture was centrifuged at 13000 rpm for 20 min, and HCl washing and re-centrifugation was repeated 3 times. Then, GO suspension was neutralized with DI water and centrifugation. The synthesized GO was obtained with a concentration of 6.3 mg mL^{-1} in DI water and kept in a cold state. GO solution was prepared by diluting the as-synthesized GO in DI water at various concentrations: 0.5, 1.0, 2.0, 3.0, and 6.3 mg mL^{-1}. The GO solution was spin-coated on cleaned ITO substrates at 3000 rpm for 60 s, and the films were immediately dried at 120 °C for 20 min. The different thicknesses of the GO layers were achieved by changing the precursor concentration of the GO solution under the same spin-coating condition.

3.1.3 Spiro-OMeTAD/WO_3 Double Layers

A spiro-OMeTAD solution was prepared by dissolving spiro-OMeTAD (80 mg), 4-tert-butylpyridine (tBP, 8.4 μL), and lithium-salt solution (54.6 μL stock solution, 156 mg Bis(trifluoromethane) sulfonimide lithium salt/1 mL acetonitrile) in 1 mL of chlorobenzene. Spiro-OMeTAD solution was dropped on the perovskite thin film and maintained for 20 s, followed by spin-coating at 2500 rpm for 40 s. The tungsten oxide bu□er layers were fabricated by solution processing from tungsten oxide nanoparticle ink (5% w/v in isopropanol) and then thermal annealing at 120 °C for 5 min in air. The different thicknesses of the WO_3 layers were achieved by changing the precursor concentration and the spin-coating condition.

3.2 Device Fabrication

3.2.1 TCO Substrate

A indium tin oxide (ITO) glass was used as a substrate for perovskite solar cells. Before the deposition of the charge transport layer, the ITO glass was cleaned with acetone, ethanol, and deionized water followed by drying with a nitrogen stream to remove impurities like oils and dust. And The substrates were treated with UV-ozone for 15 min before use.

3.2.2 $CH_3NH_3PbI_3$ Perovskite Film

The 1.5 M perovskite precursor solution containing MAI and PbI_2 (1:1 molar ratio) in anhydrous dimethylformamide (DMF):dimethyl sulfoxide (DMSO) (9:1 v/v%) was stirred for more than 2 h at room temperature. The HTL-coated substrates were transferred to a nitrogen-filled glovebox, and the perovskite precursor was spin-coated at 4000 rpm for 25 s. During the spin-coating, ethyl ether was dropped onto the spinning substrates. The samples were immediately placed on the preheated hotplate and annealed for 1 min at 65°C and then 30 min at 100°C.

3.2.3 Electron Transporting Layers and Metal Electrode

An approximately 20-nm C_{60} layer was deposited on samples by thermal

evaporation, and diluted PEIE was spin-coated on top of C_{60} at 6000 rpm for 30 s. The samples were then removed from the glovebox, and their fabrication was completed by thermally evaporating Ag electrodes under vacuum.

3.2.4 Transparent Electrode

For fabrication of a bi-facial perovskite solar cell, ITO was sputtered after PEIE coating. The Ag electrode was deposited by thermal evaporation through a patterned shadow mask to allow the devices to have a transparent conducting oxide (TCO) on both sides.

3.3 Characterizations

3.3.1 Materials Characteristics

The crystallographic properties of the charge transporting films were characterized by X-ray diffraction (XRD; model: D8 advanced, Bruker) using Cu-Kα source (λ=1.54060 Å, 40 kV, 30 mA, θ-2θ mode). The film morphology and the composition of the samples were analyzed by a scanning electron microscope (FEG-SEM; model: Merlin compact, ZEISS) equipped with an energy dispersive X-ray spectroscopy system (EDS; model: APOLLO X, EDAX) The crystalline phases and structures are analyzed by x-ray photoelectron spectroscopy (XPS, Model: SIGMA PROBE, Thermo VG, UK). Optical transmittance was measured by a UV-VIS spectrophotometer (Model: Cary5000, Agilent). The thickness of the deposited films was measured using a surface profiler (Alpha step model KLA-Tencor) and cross-sectional image of SEM. The surface profile and surface roughness of the films were examined by an atomic force microscope (AFM; model: Kelvin Probe Microscope, Park Systems NE-10). The potential of the layers was measured by SKPM (Park Systems, NX-10) and photoelectron spectroscopy in air (PESA, Riken, AC-2). Photoluminescence spectra was obtained by spectrofluorometer (Jasco, FP-8500). The water vapor transmission rate (WVTR) of the PEN substrates depending on the presence of GO deposition was measured at approximately 38 °C and 100% R.H. using Permatran-W 3/33 MA (Mocon) according to ASTM F1249. The oxygen transmission rate (OTR) was measured at

approximately 23 °C using OX-TRAN 702 (Mocon) according to ASTM D3985.

3.3.2 Photovoltaic Characteristics

The current density–voltage (*J*–V) characteristics were measured using a potentiostat (CHI 608C, CH Instruments) under AM 1.5G illumination (100 mW cm^{-2}) using a solar simulator (Peccell Technologies) and calibrated using as reference cell (PV Measurements). The conventional perovskite solar cells and bi-facial perovskite solar cells were masked with a metal aperture to define active areas of 0.14 and 0.1875 cm^2, respectively. The external quantum efficiency of the solar cells was measured using a commercial incident photon-to-current conversion efficiency (IPCE) system (Model; G1218A, PV Measurements).

3.4 Bibliography

[3.1] J. H. Kang, T. Kim, J. Choi, J. Park, Y. S. Kim, M. S. Chang, H. Jung, K. T. Park, S. J. Yang and C. R. Park, *Chemistry of Materials*, 2016, **28**, 756-764.

[3.2] S. J. Sung, J. Park, Y. S. Cho, S. H. Gihm, S. J. Yang and C. R. Park, *Carbon*, 2019, **150**, 275-283.

Chapter 4. Enhanced electrical properties of Li-doped NiO hole transporting layer in p-i-n type perovskite solar cells

4.1 Introduction

Organometal halide perovskite solar cells are very promising owing to their high and rapidly increasing conversion efficiency,[1.1-1.3] and the highest certified conversion efficiency already reached 22.1%.[1.4] A typical perovskite solar cell is consisting of stacked layers of the FTO substrate, TiO_2 nanoparticle layer, perovskite layer, spiro-OMeTAD layer, and the metal top electrode, which is known as the n–i–p type mesoscopic structure. Although champion efficiencies of the perovskite solar cells have been achieved using the n–i–p type mesoscopic structure, it has some issues for the commercialization such as high-temperature annealing of TiO_2 nanoparticle film, high materials cost of spiro-OMeTAD, hysteresis during J−V measurements, and low stability of spiro-OMeTAD.[1.5-1.7] On the other hand, the p–i–n type planar structure, consisting of a stacked layer with an inverse sequence has advantages of the negligible hysteresis effect and the low processing temperatures.[1.8, 1.9] A typical p–i–n type planar device is consisting of the TCO substrate, PEDOT:PSS hole-transporting layer, perovskite layer, PCBM electron-transporting layer, and the metal top electrode. However, it is known that PEDOT:PSS could be bad for device lifetime due to its

hydroscopic and acidic nature facilitating the decomposition of perovskite materials.[4.10] As an alternative to PEDOT, nickel oxide (NiO_x) has been attracting interest due to its large optical bandgap (3.6 eV) and deep valence band (5.4 eV), which forms a favorable energy level alignment with perovskite materials.[4.11, 4.12] In addition, the use of the inorganic NiO_x layer instead of the organic PEDOT:PSS layer should be beneficial to the stability of the perovskite solar cells. However, the resistivity of NiO_x that is significantly higher than the PEDOT:PSS may cause some issues in device performances especially associated with the series resistance of the device. Several previous studies indeed reported the lower fill factor of the NiO_x-based perovskite solar cells.[4.13, 4.14] Doping acceptors to NiO_x can alleviate the losses in fill factor and J_{sc} by modulating its conductivity, as is evidenced by the engineering the HTLs used in perovskite solar cells.[4.15, 4.16]

Here I demonstrate a Li-doped NiO_x hole-extraction layer that shows significantly improved fill factor compared with the pure NiO_x counterpart. It is also found that the annealing temperature for the NiO_x layer can be lowered by doping Li ions. However, the Li doping does not influence the photocurrent and photovoltage, leading to the increased conversion efficiency. The conductive atomic force microscope study reveals that the addition of Li ions to NiO_x significantly increases the conductivity of the NiO_x layer, and thus decreases the series resistance of the device, resulting in the increased fill factor and conversion efficiency.

4.2 Properties of Li-doped NiO

Figure 4.1 shows an energy diagram of the p–i–n type perovskite solar cell incorporating the NiO_x hole-extraction layer,[4.17] where it can be found that the valence band of NiO_x is properly positioned for extracting photoexcited holes from the light-absorption layer. In spite of the proper band alignment, however, the thickness of the NiO_x layer has to be maintained as thin as possible for minimizing the series resistance originating from the insulating property of inorganic NiO_x. For instance, it has been reported that the thickness of NiO_x should be controlled less than 10 nm for achieving good device performance.[4.18] However, it is very likely that the extremely thin NiO_x layer includes significant amount of pinholes unless it is deposited using special techniques like atomic layer deposition, leading to the shunt conductance and poor device performances.[4.19] As can be seen from the cross-sectional image (Figure 4.2), therefore, a relatively thick (~ 50 nm) NiO_x layer has been deposited in this study. The SEM image clearly shows typical stacked layers of a p-i-n type perovskite solar cell consisting of an ITO substrate (180 nm), NiO_x layer (50 nm), $CH_3NH_3PbI_3$ (215 nm), $PC_{61}BM$ (65 nm), and Ag electrode (120 nm).

Figure 4.3 shows Li 1s X-ray photoelectron spectroscopy (XPS) spectra which investigates Li-doped NiO_x film formed by 10 at% Li-added NiO_x precursor solution. The Li-doped NiO_x hole extraction layers with various Li concentration have been prepared by spin coating a NiO_x precursor solution with different amounts of lithium acetate dehydrate as lithium source on ITO substrates. The peak observed at 54.72 eV corresponds to Li and its atomic concentration is calculated to be 2.74 at%. Thus, it can

be concluded that the actual amount of Li doping is smaller than the amount of Li in the precursor solution, although there must be the linear dependence between them. The optical properties of NiO_x films with various concentration of Li have been investigated by UV-Vis spectroscopy. Figure 4.4 shows transmittance and reflectance spectra of Li-doped NiO_x films deposited on the ITO substrate with different Li concentration respectively. Both of the transmittance and reflectance spectra exhibit negligible difference depending on the amount of the Li addition, so it can be concluded that the optical properties of the devices would not be influenced by the addition of Li, either.

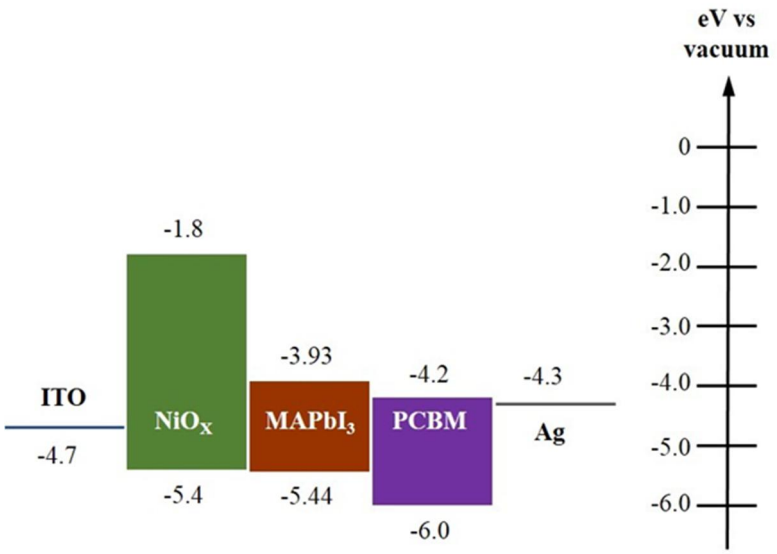

Figure 4.1 Energy diagram of p–i–n type perovskite solar cell using nickel oxide as hole extraction layer.

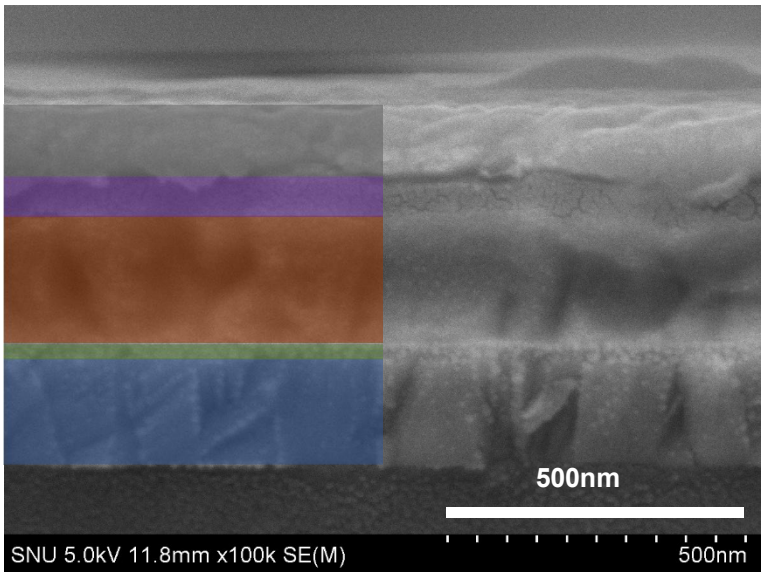

Figure 4.2 Cross-sectional SEM image of the ITO/NiO_x/$MAPbI_3$/$PC_{60}BM$/Ag electrode.

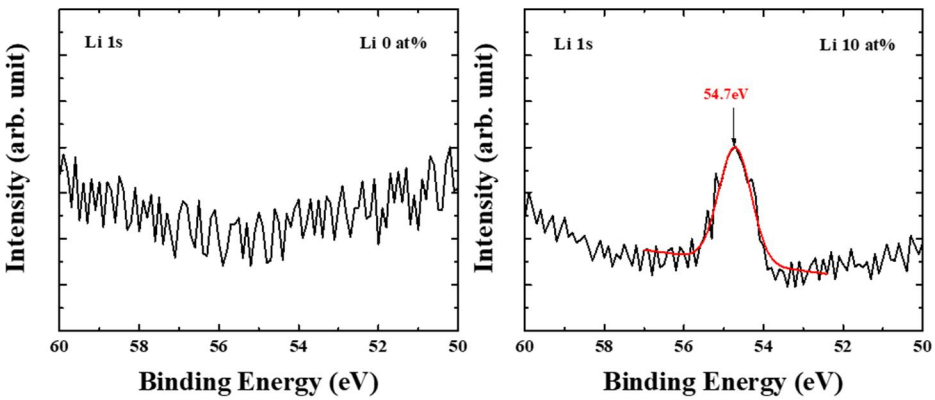

Figure 4.3 XPS spectra at the Li 1s of the NiO_x film (left) and the Li-doped NiO_x film (Right) from the narrow scan data

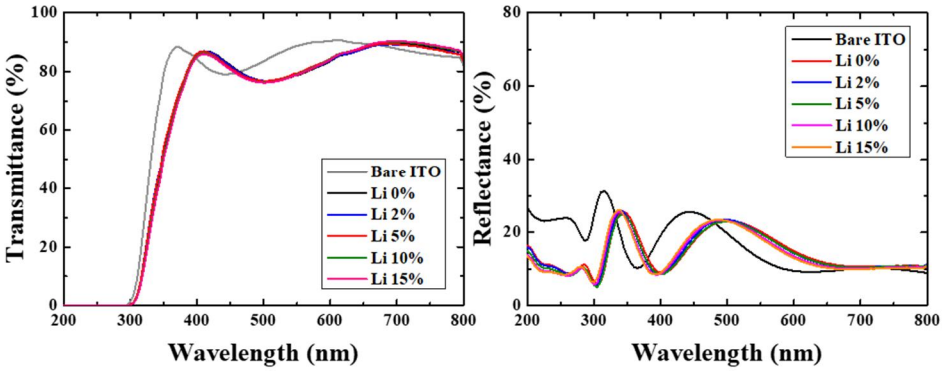

Figure 4.4 UV-Vis spectra showing the transmittance (left) and reflectance (right) of the various Li-doped NiO_x films

4.3 Photovoltaic Performances

Figure 4.5 shows the *J*−*V* curves of the NiO_x-based perovskite solar cells with different amounts of Li addition (*i.e.* Li doping), where the best device with the 5% Li-NiO_x layer shows the highest conversion efficiency of 15.41%, resulting from the J_{sc}, V_{oc}, and fill factor of 20.89 mA/cm^2, 1.00 V, and 0.74 respectively. Figure 4.6 and Table 4.1 show statistical information about the effect of the Li addition on the solar cell parameters, which shows qualitatively the same trends as the *J*−*V* curves of the best devices (Figure 4.5). The J_{sc} of the NiO_x-based devices slightly change (less than 5%) with the Li concentration, and the V_{oc} is essentially not influenced. On the other hand, the fill factor significantly increases with the Li addition up to 5 at% (from 59% to 72% in average), and then slightly decrease for higher amounts. As a result, the perovskite solar cell with the Li-doped NiO_x hole-extraction layer formed from 5 at% Li-added NiO_x precursor exhibits the highest average conversion efficiency of 14.66%, which is improved by 21% compared with the pure NiO_x hole-extraction layer.

Figure 4.7 shows the influence of the Li addition on the electrical conductivity of the NiO_x film measured by the conductive atomic force microscopy (c-AFM). All samples used for c-AFM have the same thickness of 100 nm, and the current at a bias voltage of −1.0V was measured. Assuming that the contact area by the same AFM tip is similar, the electrical conductivity of NiO_x films must be proportional to current, and it can be concluded that the resistance of the 5% sample should be the lowest. Also the series resistance of the devices calculated from the *J*−*V* curves (Fig. 3a) is the lowest for the 5% sample. The low resistance of the NiO_x layer should lead to the low series

resistance of the device, and thus to the higher fill factor of solar cells,[4.19, 4.20] which is consistent with the *J*−*V* curves (Figure 4.5). One can assume that the facilitated charge extraction at the perovskite/NiO_x interface can be another reason for the increased fill factor, which can be investigated by the PL quenching study. Figure 4.8 compares the steady state PL spectra of perovskite/NiO_x bilayer films with and without the Li doping. The PL spectra of two different samples are almost identical, indicating that the charge injection at the perovskite/NiO_x interface is not influenced by the Li doping. Therefore, it can be concluded that the increased fill factor of the Li-doped NiO_x-based device is mostly resulting from the low series resistance.[4.9, 4.21]

Table 4.1 Solar cell parameter of p–i–n type perovskite solar cells with various Li-doped NiO_x layers

Li %	J_{sc} (mA/cm^2)	V_{oc} (V)	FF	Efficiency (%)
0	20.57±0.51	1.00 ± 0.00	0.59 ± 0.03	12.15 ± 0.83
2	20.70 ± 0.68	1.00 ± 0.01	0.65 ± 0.01	13.45 ± 0.58
5	20.38 ± 0.55	1.00 ± 0.01	0.72 ± 0.02	14.66 ± 0.66
10	18.75 ± 0.53	1.03 ± 0.01	0.71 ± 0.01	13.76 ± 0.25
15	18.89 ± 0.68	1.03 ± 0.00	0.70 ± 0.00	13.66 ± 0.56

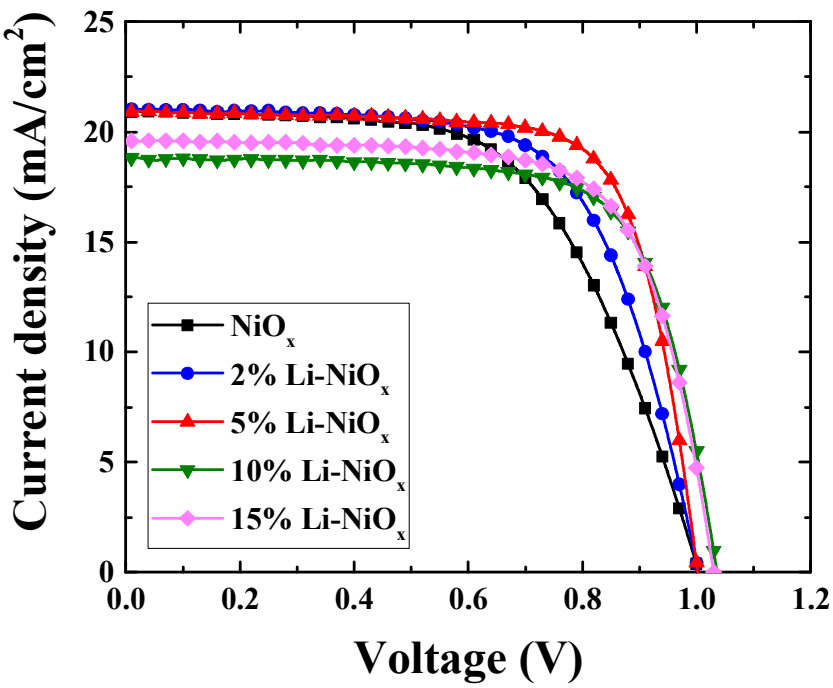

Figure 4.5 *J–V* curves of the best performing devices with various Li-doped NiO_x layers

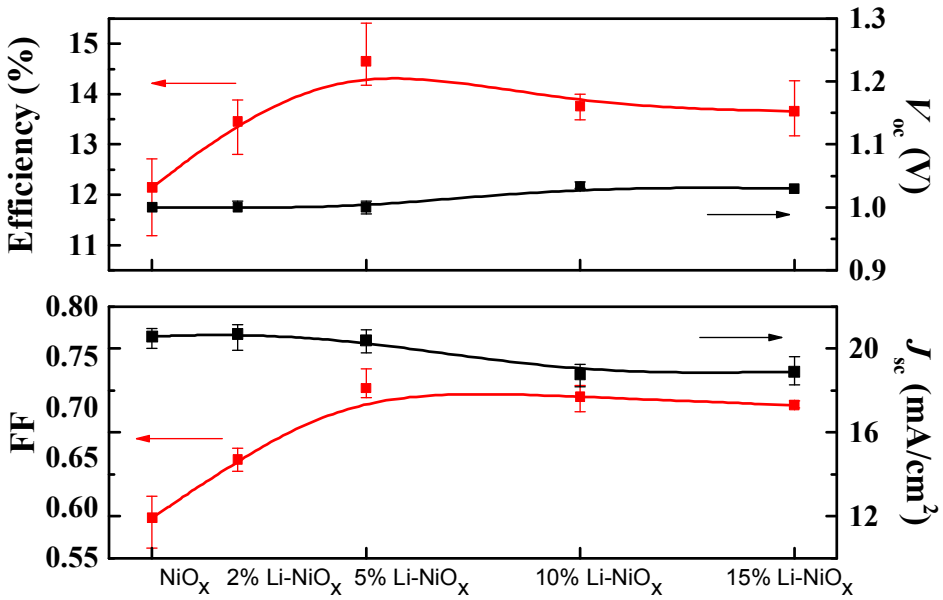

Figure 4.6 *J–V* characteristics of the perovskite solar cells with Li-doped NiO_x layers as a function of the concentration of Li

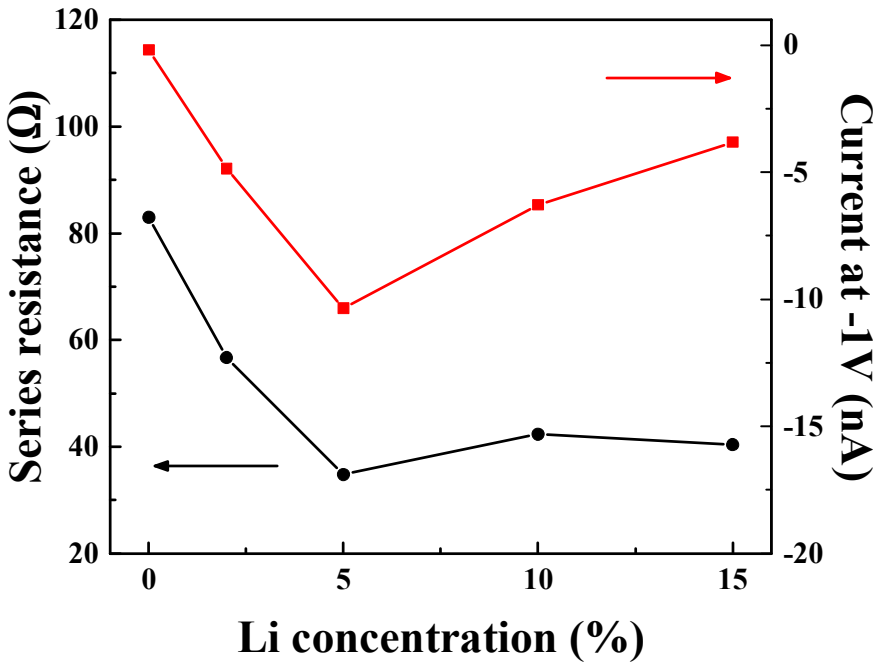

Figure 4.7 The series resistance of the devices and the electric current of various Li-doped NiO_x film at a bias potential of -1.0 V.

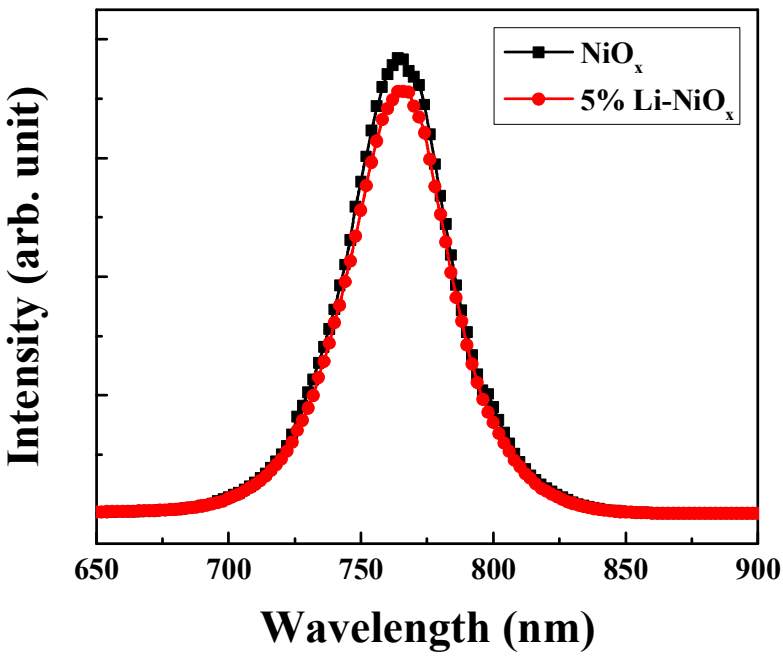

Figure 4.8 Photoluminescence spectra of the MAPbI3 on the NiO_x film and Li-doped NiO_x film form by 5 at% Li-added NiO_x precursor solution respectively. (excited by 530nm laser).

4.4 Conclusion

In summary, p–i–n type planar perovskite solar cells incorporating the Li-doped NiO_x hole-extraction layer have been demonstrated, and the influence of the Li doping on the device performance has been investigated. The fill factor of the NiO_x-based perovskite solar cell can be significantly increased by doping Li to NiO_x, while the J_{sc} and V_{oc} are merely influenced. The increased fill factor has been ascribed to the increased electrical conductivity, evidenced by the conductive AFM measurement. It should be noted that the functioning NiO_x layer could be prepared at low temperature of 200 ^{o}C. As a result, the p–i–n type planar perovskite solar cell exhibits an improved conversion efficiency of 15.41% by incorporating the low-temperature Li-doped NiO_x hole extraction layer.

4.5 Bibliography

[4.1] G. Xing, N. Mathews, S. Sun, S. S. Lim, Y. M. Lam, M. Grätzel, S. Mhaisalkar and T. C. Sum, *Science*, 2013, **342**, 344-347.

[4.2] Q. Chen, H. Zhou, Z. Hong, S. Luo, H.-S. Duan, H.-H. Wang, Y. Liu, G. Li and Y. Yang, *Journal of the American Chemical Society*, 2014, **136**, 622-625.

[4.3] S. D. Stranks, G. E. Eperon, G. Grancini, C. Menelaou, M. J. P. Alcocer, T. Leijtens, L. M. Herz, A. Petrozza and H. J. Snaith, *Science*, 2013, **342**, 341-344.

[4.4] W. S. Yang, J. H. Noh, N. J. Jeon, Y. C. Kim, S. Ryu, J. Seo and S. I. Seok, *Science*, 2015, **348**, 1234-1237.

[4.5] J. H. Heo, H. J. Han, D. Kim, T. K. Ahn and S. H. Im, *Energy & Environmental Science*, 2015, **8**, 1602-1608.

[4.6] J. Liu, Y. Wu, C. Qin, X. Yang, T. Yasuda, A. Islam, K. Zhang, W. Peng, W. Chen and L. Han, *Energy & Environmental Science*, 2014, **7**, 2963-2967.

[4.7] N.-G. Park, *The Journal of Physical Chemistry Letters*, 2013, **4**, 2423-2429.

[4.8] J. You, Z. Hong, Y. Yang, Q. Chen, M. Cai, T.-B. Song, C.-C. Chen, S. Lu, Y. Liu, H. Zhou and Y. Yang, *ACS Nano*, 2014, **8**, 1674-1680.

[4.9] P. Docampo, J. M. Ball, M. Darwich, G. E. Eperon and H. J. Snaith, *Nat Commun*, 2013, **4**.

[4.10] F. C. Krebs, T. Tromholt and M. Jorgensen, *Nanoscale*, 2010, **2**, 873-886.

[4.11] K.-C. Wang, J.-Y. Jeng, P.-S. Shen, Y.-C. Chang, E. W.-G. Diau, C.-H. Tsai, T.-Y. Chao, H.-C. Hsu, P.-Y. Lin, P. Chen, T.-F. Guo and T.-C. Wen, *Scientific Reports*, 2014, **4**, 4756.

[4.12] J. H. Kim, P.-W. Liang, S. T. Williams, N. Cho, C.-C. Chueh, M. S. Glaz, D. S. Ginger and A. K. Y. Jen, *Advanced Materials*, 2015, **27**, 695-701.

[4.13] J. Seo, S. Park, Y. Chan Kim, N. J. Jeon, J. H. Noh, S. C. Yoon and S. I. Seok, *Energy & Environmental Science*, 2014, **7**, 2642-2646.

[4.14] Z. Xiao, C. Bi, Y. Shao, Q. Dong, Q. Wang, Y. Yuan, C. Wang, Y. Gao and J. Huang, *Energy & Environmental Science*, 2014, **7**, 2619-2623.

[4.15] A. Abate, T. Leijtens, S. Pathak, J. Teuscher, R. Avolio, M. E. Errico, J. Kirkpatrik, J. M. Ball, P. Docampo, I. McPherson and H. J. Snaith, *Physical Chemistry Chemical Physics*, 2013, **15**, 2572-2579.

[4.16] W. H. Nguyen, C. D. Bailie, E. L. Unger and M. D. McGehee, *Journal of the American Chemical Society*, 2014, **136**, 10996-11001.

[4.17] I. J. Park, M. A. Park, D. H. Kim, G. D. Park, B. J. Kim, H. J. Son, M. J. Ko, D.-K. Lee, T. Park, H. Shin, N.-G. Park, H. S. Jung and J. Y. Kim, *The Journal of Physical Chemistry C*, 2015, **119**, 27285-27290.

[4.18] S. Seo, I. J. Park, M. Kim, S. Lee, C. Bae, H. S. Jung, N.-G. Park, J. Y. Kim and H. Shin, *Nanoscale*, 2016, **8**, 11403-11412.

[4.19] W. Chen, Y. Z. Wu, Y. F. Yue, J. Liu, W. J. Zhang, X. D. Yang, H. Chen, E. B. Bi, I. Ashraful, M. Gratzel and L. Y. Han, *Science*, 2015, **350**, 944-948.

[4.20] X. Xu, Z. Liu, Z. Zuo, M. Zhang, Z. Zhao, Y. Shen, H. Zhou, Q. Chen, Y. Yang and M. Wang, *Nano Letters*, 2015, **15**, 2402-2408.

[4.21] A. Abrusci, S. D. Stranks, P. Docampo, H.-L. Yip, A. K. Y. Jen and H. J. Snaith, *Nano Letters*, 2013, **13**, 3124-3128.

Chapter 5. Bi-functional Graphene Oxide Hole-Transporting and Barrier Layer for Transparent Bi-facial Flexible Perovskite Solar Cells

5.1 Introduction

In the approximately 10 years since methylammonium lead iodide (MALI) and methylammonium lead bromide (MALBr) were first introduced as visible-light sensitizers for photovoltaic cells,[5.1] the maximum efficiency of organic–inorganic hybrid perovskite solar cells has reached ~25.2%.[5.2] This high efficiency in a short period is attributed to the outstanding properties of organic–inorganic hybrid perovskite materials, including their high absorption coefficients,[5.3, 5.4] long charge-carrier lifetime,[5.5-5.9] large diffusion length,[5.8-5.12] and ambipolar transport properties.[5.13-15] Perovskite solar cells with the certified high efficiency generally possess the n-i-p structure used in dye-sensitized solar cells;[5.16-5.21] however, the high-temperature processing of n-type materials and the chemical instability of p-type materials have limited the various selection of materials and the device geometry.[5.4, 5.18, 5.22, 5.23] On the other hand, perovskite solar cells with the p-i-n structure can be applied in various forms without being limited by the materials selection as the charge-transport materials are processed at a relatively low temperature.[5.24-27]

In the p-i-n structure, the incident light reaches the perovskite absorption layer

through the p-type materials; therefore, high transparency of p-type materials is required. Considering the manufacturing process, deposition of the top layer over the p-type material requires a physically and chemically durable p-type material.[5.24] In addition, p-type materials must have a proper band alignment with the perovskite material to achieve efficient hole extraction from the perovskite layer.[5.28] Although poly(3,4-ethylenedioxythiophene) polystyrene sulfonate (PEDOT:PSS) is the most commonly used p-type hole transport material (HTM), its acidic and hygroscopic properties and electrical inhomogeneity have been critical issues for the stability of the perovskite solar cells.[5.29, 5.30] P-type oxide materials such as NiO have also been studied; however, their use is limited by the required high-temperature.[5.31-5.35] Therefore, there have been continuous efforts to identify new HTMs that can overcome the limitations, and the graphene oxide (GO) has emerged as a potential alternative to the conventional HTMs.[5.36] GO has advantages of low cost and good stability, but it has suffered from the issue of low conductivity.[5.37] So far, thus, GO has used either in the mixture form with conventional p-type materials (e.g. PEDOT:PSS and oxides),[5.38-5.42] or with the chemical modifications like attaching functional groups,[5.43-5.46] and chemical reduction.[5.47, 5.48] This process, however, complicates the manufacturing process and offsets the economic benefits of using GO.

In this study, we demonstrate that the GO layer with the appropriate thickness can exhibit high transmittance, extract holes efficiently from the perovskite layer, and block water/oxygen permeation from the substrate, indicating that GO can be used as a good HTM of the perovskite solar cells. In particular, the barrier properties of the GO layer successfully compensate the relatively high water/oxygen permeability of the

polyethylene naphthalate (PEN) substrates, and significantly improve the long-term stability of the flexible perovskite solar cells. In addition, transparent perovskite solar cells are prepared by replacing the conventional Ag top electrode with the indium tin oxide (ITO) top electrode, enabling the bi-facial light illumination, thereby allowing various new optoelectronic applications of perovskite materials such as high-efficiency tandem solar cells, building-integrated photovoltaics (BIPVs), and displays.

5.2 Properties of Graphene Oxide Layer

Figure 5.1 presents a schematic diagram of a perovskite solar cell with p–i–n structure. A graphene oxide (GO) hole-transporting layer (HTL) was deposited on an ITO-coated substrate, followed by the sequential deposition of a perovskite light absorbing layer, electron transport layer, and a metal electrode. A poly(3,4-ethylenedioxythiophene) polystyrene sulfonate (PEDOT:PSS) HTL was used for a comparison without modifying the other components. NiO-based HTLs which generally exhibit better performances than the PEDOT:PSS counterpart cannot be used due to the limited processing temperature of the plastic substrate. Both of the GO and PEDOT:PSS HTLs were annealed at relatively low temperature of 120 °C. Three major requirements for the good HTL are the photon transmission, electron blocking, and the hole extraction/transport. Firstly, the photon transmission capability of the GO HTL layer has been investigated by the UV-Vis spectroscopy. Figure 5.2 shows the transmittance spectra of GO-HTL-coated ITO/glass substrates with various thicknesses of the GO HTL, where the thickness was changed by changing the concentration of the GO coating solution (0.5, 1.0, 2.0, 3.0, and 6.3 mg mL^{-1} at 3000 rpm). Given that the bandgap of $CH_3NH_3PbI_3$ is 1.55 eV,[5.49] the transmittance of the HTL layer under 800 nm is particularly important for preventing the parasitic absorption losses. The transmittance of the GO-coated ITO substrates decreases with the increasing concentration, but most of the samples exhibit good enough transmittance (> 90%) over the whole range of the wavelength except for the highest concentration of 6.3 mg mL−1. Secondly, the electron

blocking capability of the GO HTL has been studied. The uniformity of the GO layer is very important for efficient blocking of the back electron transfer or the leakage current. Considering the roughness (R_{rms}) of the ITO substrate (4.6 nm, Figure 5.3(a)) and the thickness of the GO monolayer (~ 1nm),[5.50] the uniform coverage of the ITO substrate by the GO layer has to be confirmed. Figure 5.4 displays the surface properties of a typical GO-coated ITO substrate (0.5 mg mL−1, 3000 rpm). The surface morphology observed in the high-resolution FE-SEM image (left in Figure 5.4) is similar to that of the bare ITO substrate, but clear contrast between dark (or thick) and bright (or thin) parts can also be found. The SKPM study was performed for further investigating the differences and for confirming the complete coverage by the GO layer. The AFM topology (center in Figure 5.4) of the same sample (different area from the SEM image) shows a clear step of approximately 16 nm, which is consistent with the SEM analysis. However, the potential mapping at the same spot (right in Figure 5.4) shows no contrast at all with a measured work function of 5.02 eV (cf. 4.83 eV for bare ITO, Figure 5.3(b)), so it can be concluded that the ITO substrate is completely covered by the same material. The photoelectron spectroscopy in air (PSEA) measurement shown in Figure 5.5 reveals that the work function values of bare and GO-coated ITO substrate are 4.97 and 5.29 eV, respectively. Therefore, it can be concluded that the GO layer consisting of multilayer GO flakes is completely covering the ITO substrate. It is noteworthy that the Rrms of GO-coated ITO substrate (4.2~4.6 nm) remains almost same as that of bare ITO substrate (4.6 nm), while that of PEDOT:PSS-coated ITO substrate is significantly smaller (2.4 nm, Figure 5.3(c)). Thirdly, the hole extraction capability of the GO HTL has been investigated by the PL quenching study. Figure 5.6 compared the steady-state PL spectra

(excitation at 530 nm) of the MALI perovskite layer deposited on the ITO substrate with various HTLs. PEDOT:PSS is a well-known HTL material with a proper band alignment with MALI, so the PL peak is quenched almost completely. Similarly, the GO HTL also exhibits excellent PL quenching, confirming the proper band alignment with MALI. Therefore, it can be concluded that the GO layer in this study can be used for the HTL of the perovskite solar cells.

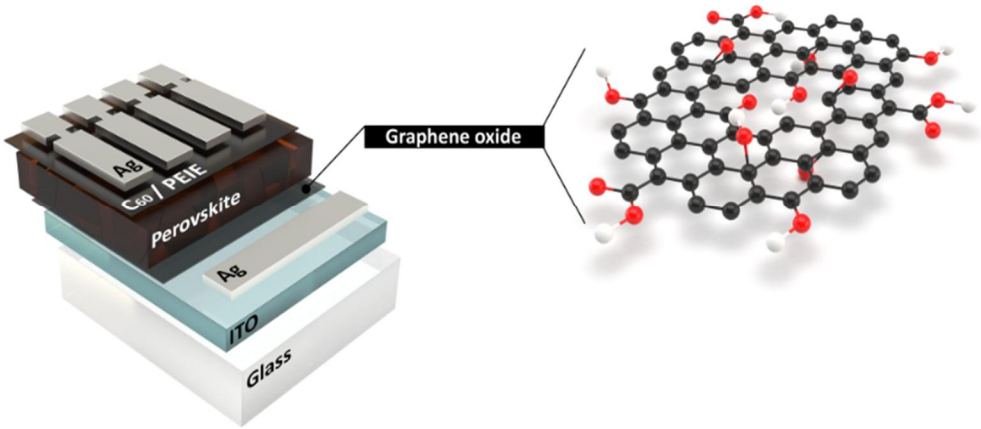

Figure 5.1 Schematic structure of a typical perovskite solar cell with a GO HTL

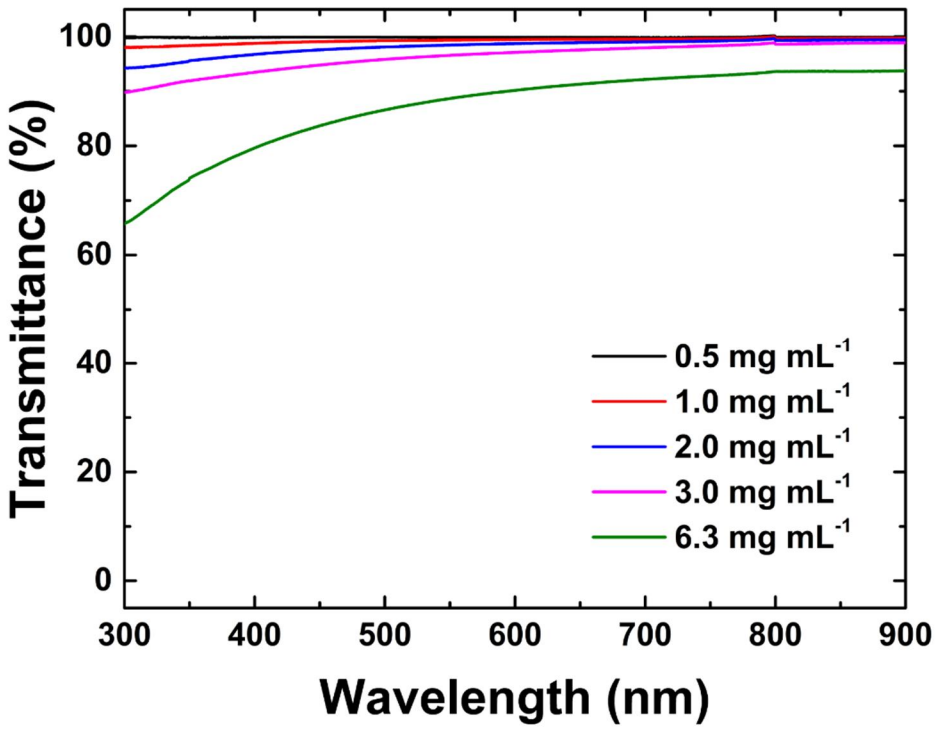

Figure 5.2 Transmittance spectra of glass/ITO/GO samples with different concentrations of GO coating solutions.

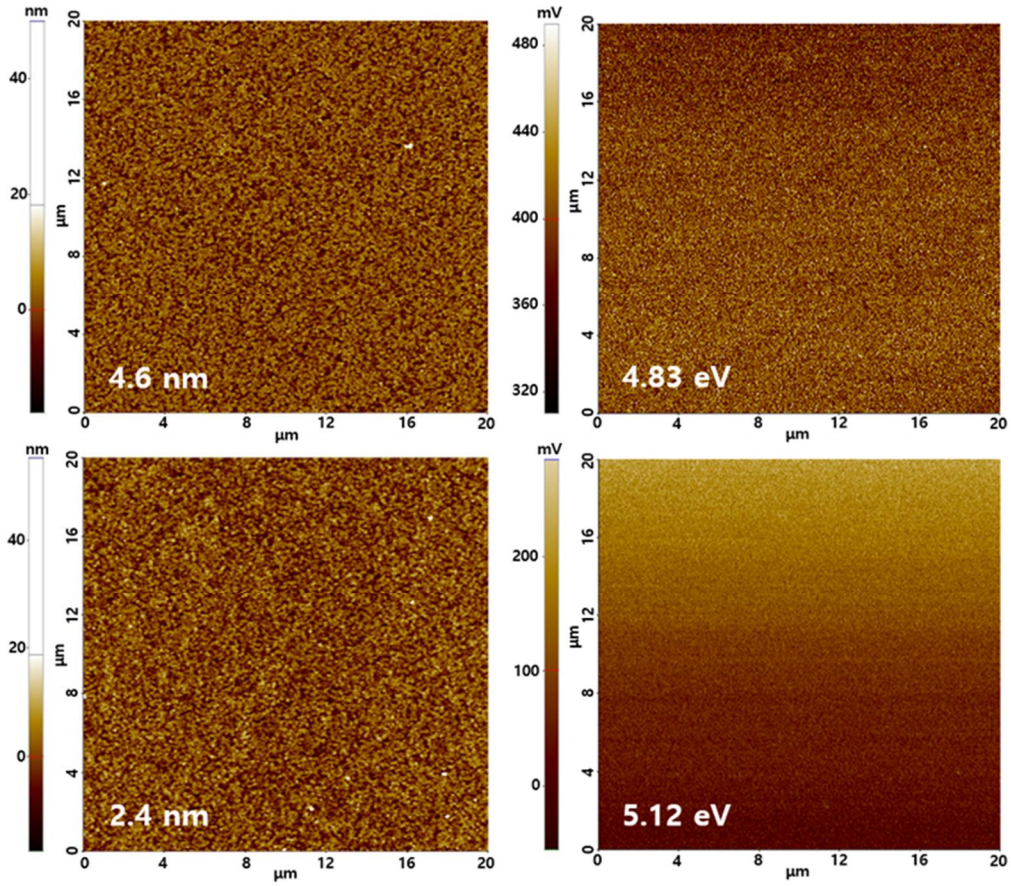

Figure 5.3 (a) AFM topography and (b) potential mapping images of a bare ITO substrate. (c) AFM topography and (c) potential mapping images of a PEDOT:PSS-coated ITO substrate

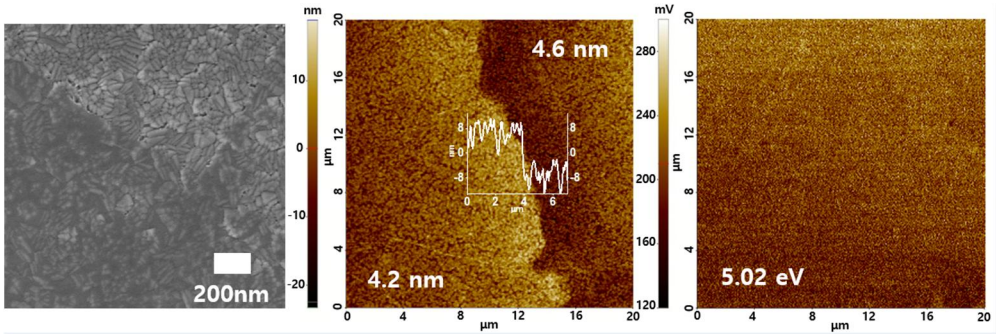

Figure 5.4 SEM (left), AFM topography (middle), and potential mapping (right) images of the glass/ITO/GO sample (concentration of 0.5 mg mL^{-1}).

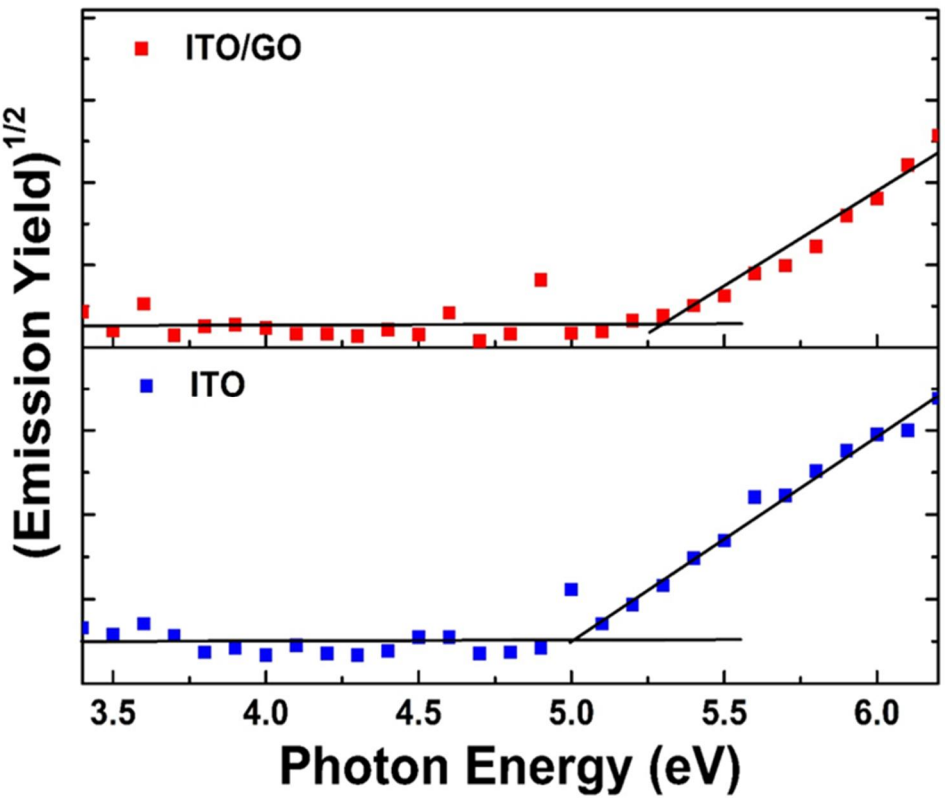

Figure 5.5 Photoelectron emission spectra of the ITO/GO and bare ITO substrates

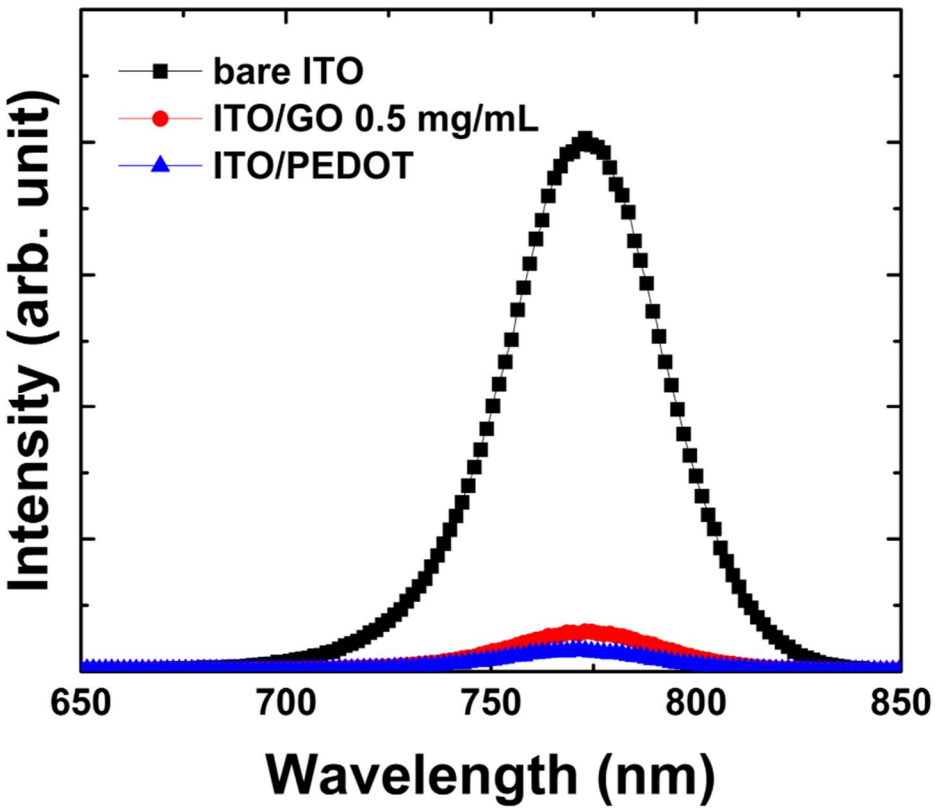

Figure 5.6 Steady-state PL spectra of perovskite layers deposited on various substrates.

5.3 Perovskite Solar Cell with GO HTL

Figure 5.7 and Table 5.1 present the statistical photovoltaic (PV) performances of perovskite solar cells as a function of the GO solution concentration (spin coating at 4000 rpm). The average short-circuit current density (J_{sc}) of the perovskite solar cell increases from 11.53 to 18.19 mA cm^{-2} with decreasing GO solution concentration from 6.3 to 0.5 mg mL^{-1}. The increased J_{sc} can be mainly ascribed to the higher transmittance of thinner GO HTLs. The open-circuit voltage (V_{oc}) is barely influenced by the HTL thickness except for the slight reduction of the thinnest HTL. Fill factor increases with the decreasing solution concentration (*i.e.* HTL thickness), which is a consequence of the reduced series resistance (R_s) as observed from the stiffer slope of $J-V$ curves of thinner HTLs near V_{oc} (Figure 5.8). As a result, the perovskite solar cells with the thinnest GO HTL exhibit the highest average conversion efficiency of 11.98% (best efficiency of 12.31%). This observation shows that the hole transport across the GO HTL can cause a series resistance issue due to its low conductivity, and thus reducing its thickness while maintaining the uniform coverage is important for achieving good PV performances. Therefore, the device performances with lower concentrations (*i.e.* 0.5 and 1.0 mg mL^{-1}) are further optimized by changing the spin coating speed from 4000 to 3000 rpm. The statistical PV performances are summarized in Table 1, and the $J-V$ curves of the devices with efficiencies close to the average value of each coating condition are presented in Figure 5.9. In general, thinner HTLs (*i.e.* lower concentration and higher spinning rate) lead to the better performances. However, the devices with the HTL

prepared with the condition of 0.5 mg mL^{-1} at 3000 rpm exhibit slightly better efficiency (average efficiency of 12.31%) with better reproducibility, so the same condition has been used for preparing flexible and transparent solar cells.

Table 5.1 Photovoltaic parameters of perovskite solar cells as a function of GO concentration.

Concentration	J_{sc} (mA cm^{-2})	V_{oc} (V)	Efficiency (%)	FF
6.3 mg mL^{-1}	11.53±1.71	0.90±0.02	6.17±1.33	0.60±0.10
3.0 mg mL^{-1}	14.96±0.68	0.89±0.01	8.71±1.00	0.66±0.05
2.0 mg mL^{-1}	15.87±0.39	0.91±0.01	10.00±0.23	0.69±0.03
1.0 mg mL^{-1}	16.69±0.55	0.90±0.02	11.41±0.25	0.76±0.02
0.5 mg mL^{-1}	18.19±0.46	0.86±0.02	11.98±0.49	0.77±0.03

Table 5.2 Photovoltaic parameters of perovskite solar cells as a function of GO concentration and spin-coating speed.

	J_{sc} (mA cm^{-2})	V_{oc} (V)	Efficiency (%)	FF
1.0 mg mL^{-1}, 3000rpm	16.68±0.40	0.83±0.02	9.27±1.24	0.67±0.09
1.0 mg mL^{-1}, 4000rpm	16.81±0.37	0.85±0.01	11.03±0.37	0.77±0.01
0.5 mg mL^{-1}, 3000rpm	18.36±0.43	0.85±0.02	12.31±0.24	0.79±0.01
0.5 mg mL^{-1}, 4000rpm	18.19±0.46	0.86±0.02	11.98±0.49	0.77±0.03

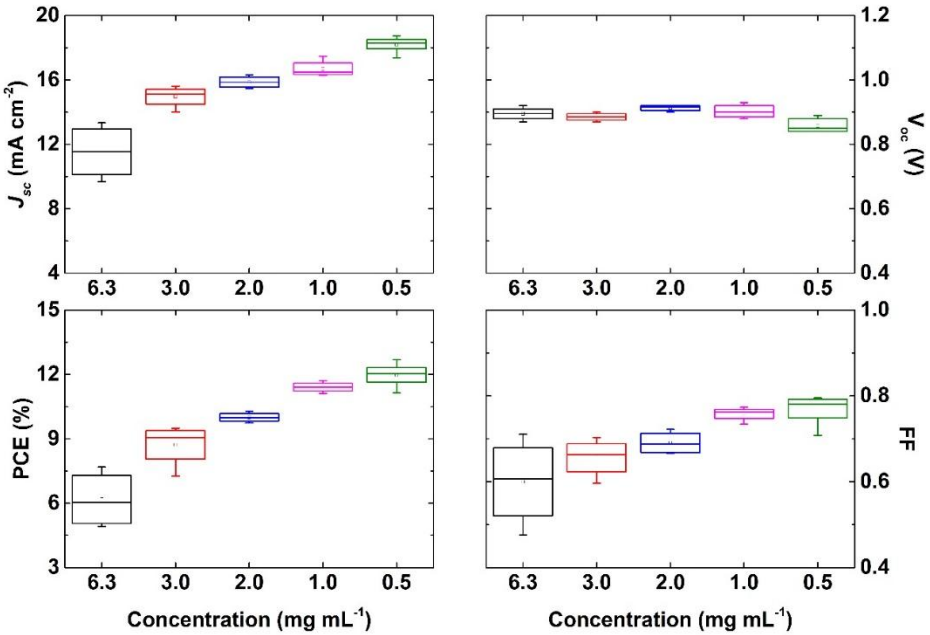

Figure 5.7 Statistical characteristics of perovskite solar cells with various concentrations of GO solutions.

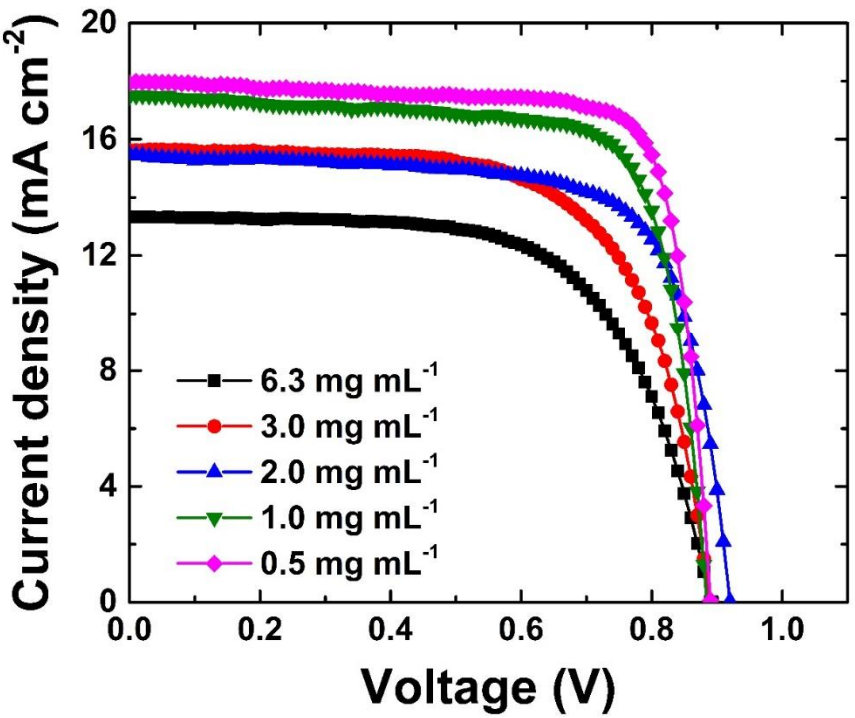

Figure 5.8 Optimal J-V curves of perovskite solar cells with various concentrations of GO solutions.

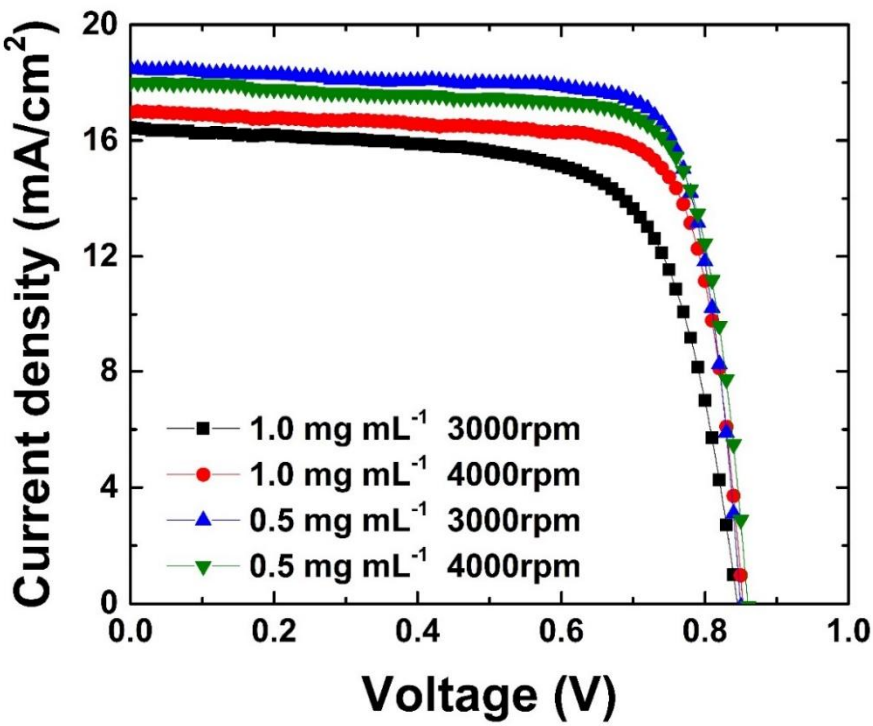

Figure 5.9 *J-V* curves of perovskite solar cells with various preparation conditions.

5.4 Transparent and Flexible Perovskite Solar Cell with GO HTL

Figure 5.10 shows the $J-V$ curves of the transparent perovskite solar cells with various HTLs (GO *vs.* PEDOT:PSS) and substrates (PEN *vs.* glass), and the solar cell parameters are summarized in Table 5.3 (light illumination from the substrate side). Transparent devices have been prepared by replacing the conventional Ag electrode with a sputtered ITO electrode (Figure 5.11). It should be noted that the J_{sc} of transparent devices is not as good as the non-transparent counterparts probably due to the absence of the light reflection by the Ag top electrode. The flexible devices with the ITO-coated plastic (polyethylene naphthalate; PEN) substrates exhibit lower J_{sc} regardless of the HTL materials owing to the low transmittance (Figure 5.12). From the transmittance spectra of the ITO-coated PEN (red squares) and glass (blue circles) substrates, the theoretical maximum J_{sc} that can be obtained from the substrate has been calculated by assuming 100% internal quantum efficiency (IQE). The maximum J_{sc} values that can be obtained with the ITO-coated PEN and glass substrates are 20.57 and 22.23 mA cm^{-2}, respectively. The amounts of J_{sc} reduction for the GO and PEDOT:PSS HTLs are 9% (from 15.41 to 14.01 mA cm^{-2}) and 21% (from 17.46 to 13.74 mA cm^{-2}), respectively, which is qualitatively consistent with the theoretical calculation (7.5%). In addition, the sheet resistance of the commercial ITO/PEN substrate (13.9 ohms/□) is higher than the ITO/glass substrate (6.6 ohms/□), leading to the higher R_s of the PEN-based devices. One of the biggest advantages of having transparent solar cells is that they can be illuminated through both sides (*i.e.* front-side illumination through the top electrode and back-side

illumination through the substrate), which is crucial for some promising applications like the bi-facial solar cells. Figure 5.13 displays the effects of the illumination direction on the PV performance of the transparent perovskite solar cells with the GO/ITO/glass substrates. The V_{oc} (0.95 V) and fill factor (0.75, 0.76) are not influenced by the direction of the light illumination, but the J_{sc} under the front-side illumination through the top electrode (17.91 mA cm^{-2}) is higher than the back-side counterpart (16.68 mA cm^{-2}) by approximately 7.4%. As a result, the transparent perovskite solar cell exhibits a higher conversion efficiency of 12.48% with the front-side illumination compared with the back-side illumination (11.45%). The V_{oc} and fill factor from the same device are likely to be constant regardless of the illumination direction. Different profiles of light absorption and the resulting photoelectron density may influence the charge-collection properties, but it is not likely to happen in this study due to the thin thickness of the perovskite layer. On the other hand, the J_{sc} must depend on the direction of the light illumination, because the light-harvesting properties are directly affected by the light absorption by the perovskite layer. Under the back-side illumination, the incident photons should pass through three layers (*i.e.* glass substrate, ITO layer, and HTL) before reaching the perovskite layer, but they need to pass through only two layers (*i.e.* sputtered ITO and ETL) under the front-side illumination. Therefore, there are better chances of photon losses by the parasitic absorption during the back-side illumination. In addition, the reflection losses might be larger during the back-side illumination due to the smoother and highly reflective surface of the glass substrate.

Table 5.3 Photovoltaic parameters of transparent perovskite solar cells with various HTLs and substrates.

	J_{sc} (mA cm^{-2})	V_{oc} (V)	Efficiency (%)	FF
GO/Glass	15.41	0.92	11.39	0.80
GO/PEN	14.01	0.95	9.34	0.70
PEDOT/Glass	17.46	0.90	11.35	0.72
PEDOT/PEN	13.74	0.95	10.11	0.77

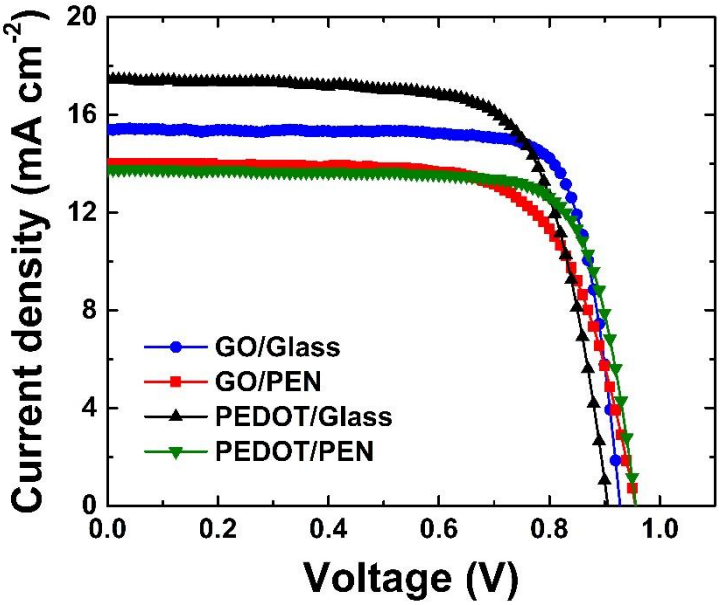

Figure 5.10 Optimal *J-V* curves of perovskite solar cells with various concentrations of GO solutions.

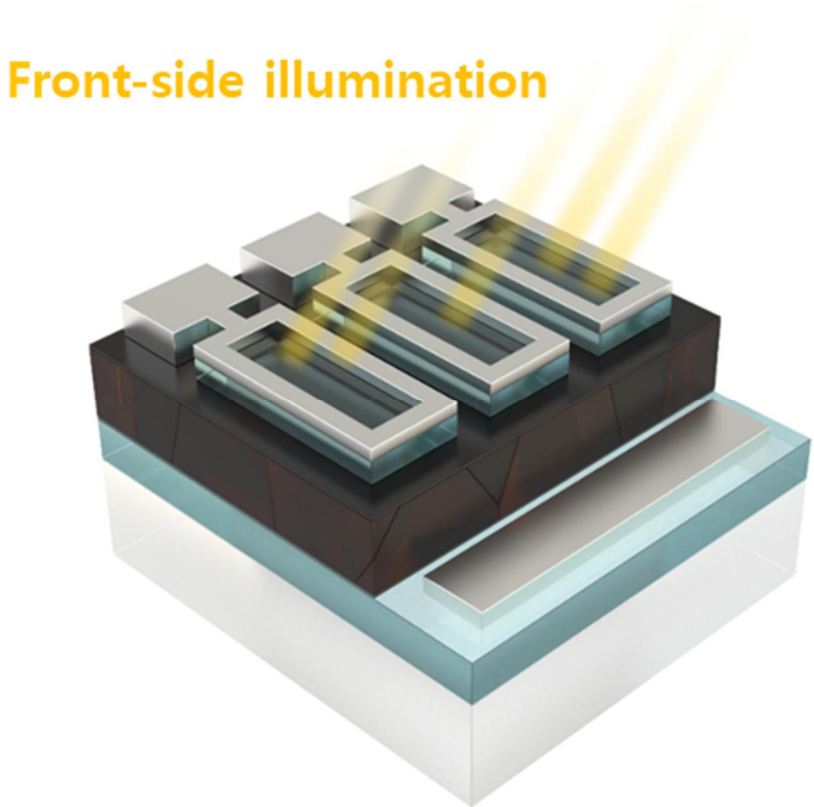

Figure 5.11 A schematic structure of a typical transparent perovskite solar cell.

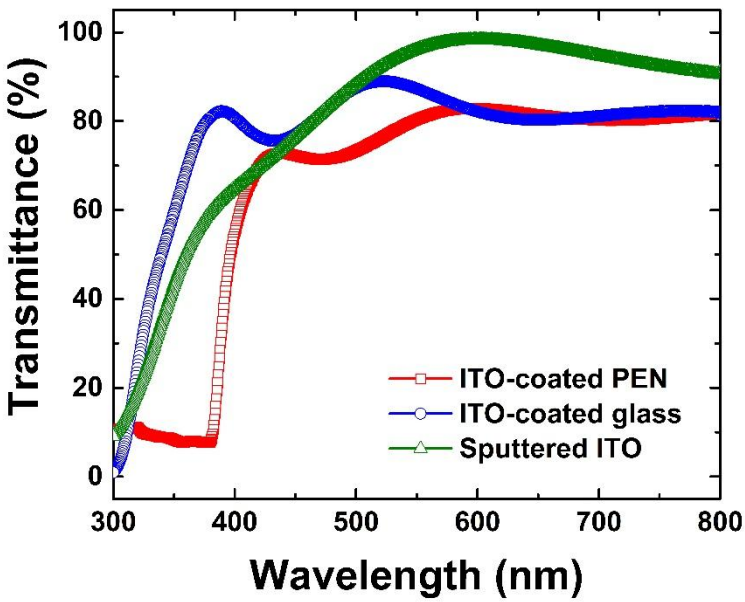

Figure 5.12 Transmittance spectra of sputtered ITO layers prepared on various substrates.

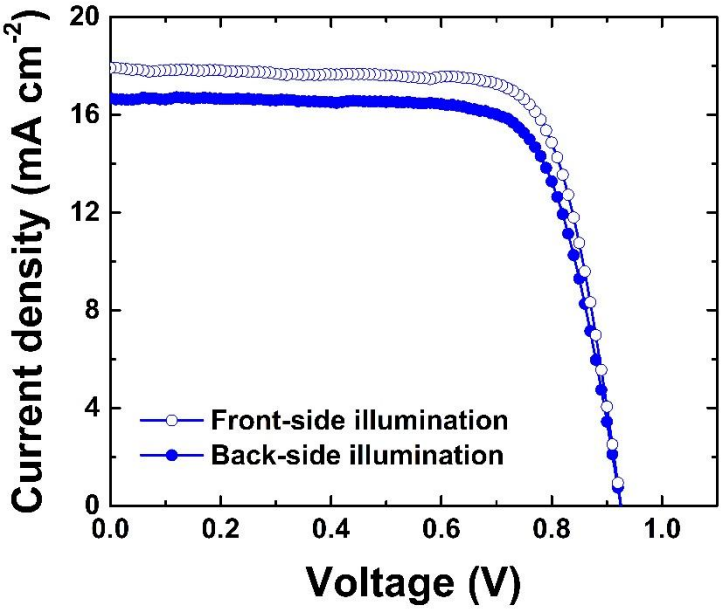

Figure 5.13 *J–V* curves of transparent perovskite solar cells with GO HTLs with different directions of light illumination.

5.5 Bi-functional GO Layer

Figure 5.14 compares the long-term stability of the perovskite solar cells with different substrates and HTLs (*i.e.* PEN *vs.* glass substrates and GO *vs.* PEDOT:PSS HTLs). For the long-term stability test, the devices have been stored in ambient atmosphere without the encapsulation layer, and the $J-V$ curves have been measured approximately in every 24 hours under the back-side illumination through the substrate. The devices with the PEDOT:PSS HTL and PEN substrate (blue hollow circles) degrade very quickly mostly due to the decrease in J_{sc}. Devices with the glass substrates (blue solid circles) are relatively stable than those with the PEN substrates, but PEDOT-PSS-based devices are very unstable regardless of the substrates, showing a lifetime no more than 2 days. Instability of the perovskite solar cells with the PEDOT:PSS HTL can be attributed to the acidic and hydroscopic nature of the PEDOS:PSS, and the instability issue is more significant with the PEN substrate due to the higher water/oxygen permeability than the glass substrate.[5.51] On the other hand, the perovskite solar cells with the GO HTL exhibit much improved long-term stability, maintaining more than 90% of their initial conversion efficiencies for 120 h. More importantly, the GO-based devices with the PEN substrate exhibit comparable long-term stability to those with the glass substrate, indicating that the excellent barrier properties of the GO HTL effectively compensate the higher permeability of the PEN substrate. Figure 5.15 shows the water/oxygen permeability (WVTR/OTR) of the GO-coated ITO/PEN substrates as a function of the GO solution concentration (*i.e.* GO layer thickness). Both of the WVTR

and OTR monotonically decrease with the increasing thickness, indicating that the barrier properties are improved. It should be noted that the measured WVTR of the bare ITO/PEN substrate (0.37 g m^{-2} day^{-1}) is significantly lower than the known values of the PEN (7.3 g m^{-2} day^{-1})[5.51], suggesting that the inorganic ITO layer already functions as a primary barrier layer. The WVTR of the ITO/PEN substrate decreases to 0.31 g m^{-2} day^{-1} with the GO HTL (0.5 mg mL^{-1}; same condition used in this study), and further decreases to 0.10 g m^{-2} day^{-1} with the thicker GO layer (2.0 mg mL^{-1}). The OTR values also show the same dependency on the GO layer thickness. Considering that the water is one of the major causes for the performance degradation of the perovskite solar cells, the enhanced long-term stability even with the flexible PEN substrate can be ascribed to the barrier properties of the GO HTL. Therefore, it can be concluded that the highly transparent GO layer with the bi-functionality of hole extraction and water/gas barrier is a promising candidate for the HTL of the efficient and stable transparent perovskite solar cells.

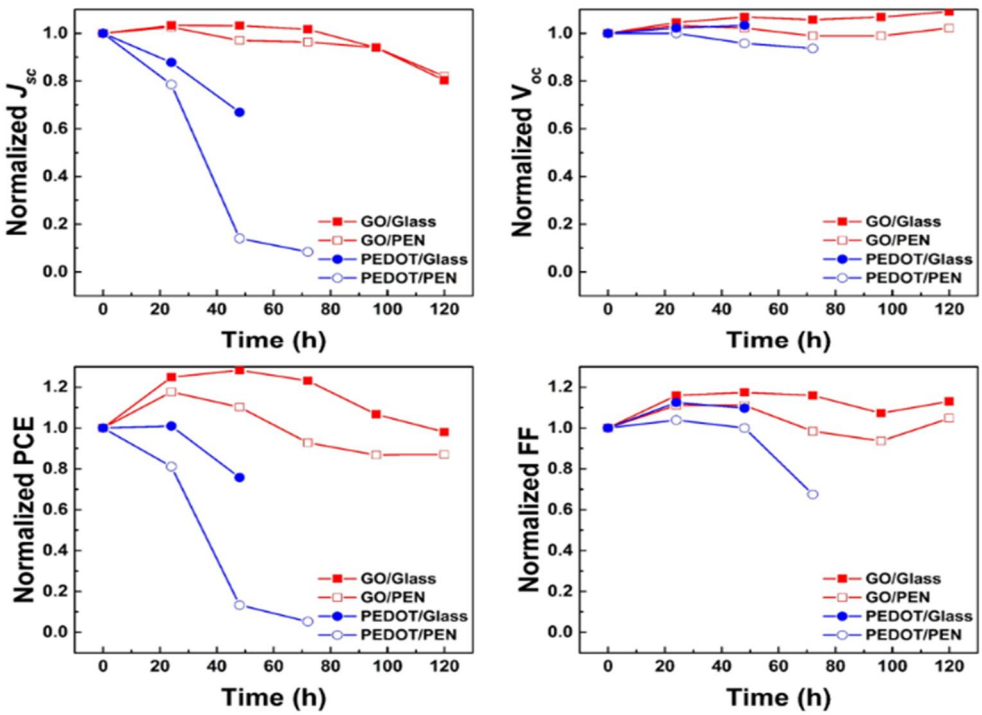

Figure 5.14 Long-term stability of transparent perovskite solar cells.

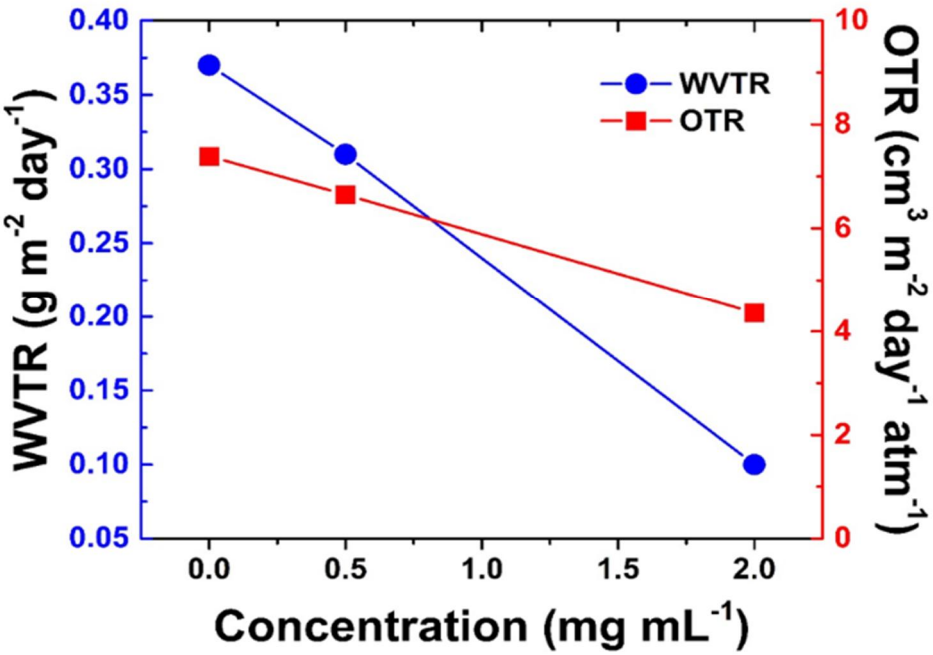

Figure 5.15 WVTR and OTR of a GO-coated PEN/ITO substrate.

5.6 Conclusion

Figure 5.14 compares the long-term stability of the perovskite solar cells with different substrates and HTLs (*i.e.* PEN *vs.* glass substrates and GO *vs.* PEDOT:PSS HTLs). For the long-term stability test, the devices have been stored in ambient atmosphere without the encapsulation layer, and the $J-V$ curves have been measured approximately in every 24 hours under the back-side illumination through the substrate. The devices with the PEDOT:PSS HTL and PEN substrate (blue hollow circles) degrade very quickly mostly due to the decrease in J_{sc}. Devices with the glass substrates (blue solid circles) are relatively stable than those with the PEN substrates, but PEDOT-PSS-based devices are very unstable regardless of the substrates, showing a lifetime no more than 2 days. Instability of the perovskite solar cells with the PEDOT:PSS HTL can be attributed to the acidic and hydroscopic nature of the PEDOS:PSS, and the instability issue is more significant with the PEN substrate due to the higher water/oxygen permeability than the glass substrate.[5.51] On the other hand, the perovskite solar cells with the GO HTL exhibit much improved long-term stability, maintaining more than 90% of their initial conversion efficiencies for 120 h. More importantly, the GO-based devices with the PEN substrate exhibit comparable long-term stability to those with the glass substrate, indicating that the excellent barrier properties of the GO HTL effectively compensate the higher permeability of the PEN substrate. Figure 5.15 shows the water/oxygen permeability (WVTR/OTR) of the GO-coated ITO/PEN substrates as a

function of the GO solution concentration (*i.e.* GO layer thickness). Both of the WVTR and OTR monotonically decrease with the increasing thickness, indicating that the barrier properties are improved. It should be noted that the measured WVTR of the bare ITO/PEN substrate (0.37 g m^{-2} day^{-1}) is significantly lower than the known values of the PEN (7.3 g m^{-2} day^{-1})[5.51], suggesting that the inorganic ITO layer already functions as a primary barrier layer. The WVTR of the ITO/PEN substrate decreases to 0.31 g m^{-2} day^{-1} with the GO HTL (0.5 mg mL^{-1}; same condition used in this study), and further decreases to 0.10 g m^{-2} day^{-1} with the thicker GO layer (2.0 mg mL^{-1}). The OTR values also show the same dependency on the GO layer thickness. Considering that the water is one of the major causes for the performance degradation of the perovskite solar cells, the enhanced long-term stability even with the flexible PEN substrate can be ascribed to the barrier properties of the GO HTL. Therefore, it can be concluded that the highly transparent GO layer with the bi-functionality of hole extraction and water/gas barrier is a promising candidate for the HTL of the efficient and stable transparent perovskite solar cells.

5.7 Bibliography

[5.1] A. Kojima, K. Teshima, Y. Shirai and T. Miyasaka, *Journal of the American Chemical Society*, 2009, **131**, 6050-6051.

[5.2] N. J. Jeon, J. H. Noh, W. S. Yang, Y. C. Kim, S. Ryu, J. Seo and S. I. Seok, *Nature*, 2015, **517**, 476-480.

[5.3] Y. Wang, Y. Zhang, P. Zhang and W. Zhang, *Physical Chemistry Chemical Physics*, 2015, **17**, 11516-11520.

[5.4] J.-H. Im, C.-R. Lee, J.-W. Lee, S.-W. Park and N.-G. Park, *Nanoscale*, 2011, **3**, 4088-4093.

[5.5] D. W. de Quilettes, S. M. Vorpahl, S. D. Stranks, H. Nagaoka, G. E. Eperon, M. E. Ziffer, H. J. Snaith and D. S. Ginger, *Science*, 2015, **348**, 683-686.

[5.6] D. Zhao, Y. Yu, C. Wang, W. Liao, N. Shrestha, C. R. Grice, A. J. Cimaroli, L. Guan, R. J. Ellingson, K. Zhu, X. Zhao, R.-G. Xiong and Y. Yan, *Nature Energy*, 2017, **2**, 17018.

[5.7] H. Zhou, Q. Chen, G. Li, S. Luo, T.-b. Song, H.-S. Duan, Z. Hong, J. You, Y. Liu and Y. Yang, *Science*, 2014, **345**, 542-546.

[5.8] Y. Chen, H. T. Yi, X. Wu, R. Haroldson, Y. N. Gartstein, Y. I. Rodionov, K. S. Tikhonov, A. Zakhidov, X. Y. Zhu and V. Podzorov, *Nature Communications*, 2016, **7**, 12253.

[5.9] S. D. Stranks, G. E. Eperon, G. Grancini, C. Menelaou, M. J. P. Alcocer, T.

Leijtens, L. M. Herz, A. Petrozza and H. J. Snaith, *Science*, 2013, **342**, 341-344.

[5.10] D. Shi, V. Adinolfi, R. Comin, M. Yuan, E. Alarousu, A. Buin, Y. Chen, S. Hoogland, A. Rothenberger, K. Katsiev, Y. Losovyj, X. Zhang, P. A. Dowben, O. F. Mohammed, E. H. Sargent and O. M. Bakr, *Science*, 2015, **347**, 519-522.

[5.11] Y. Zhao, A. M. Nardes and K. Zhu, *The Journal of Physical Chemistry Letters*, 2014, **5**, 490-494.

[5.12] A. A. Zhumekenov, M. I. Saidaminov, M. A. Haque, E. Alarousu, S. P. Sarmah, B. Murali, I. Dursun, X.-H. Miao, A. L. Abdelhady, T. Wu, O. F. Mohammed and O. M. Bakr, *ACS Energy Letters*, 2016, **1**, 32-37.

[5.13] J. M. Ball, M. M. Lee, A. Hey and H. J. Snaith, *Energy & Environmental Science*, 2013, **6**, 1739-1743.

[5.14] G. Giorgi, J.-I. Fujisawa, H. Segawa and K. Yamashita, *The Journal of Physical Chemistry Letters*, 2013, **4**, 4213-4216.

[5.15] F. Li, C. Ma, H. Wang, W. Hu, W. Yu, A. D. Sheikh and T. Wu, *Nature Communications*, 2015, **6**, 8238.

[5.16] W. S. Yang, J. H. Noh, N. J. Jeon, Y. C. Kim, S. Ryu, J. Seo and S. I. Seok, *Science*, 2015, **348**, 1234-1237.

[5.17] W. S. Yang, B.-W. Park, E. H. Jung, N. J. Jeon, Y. C. Kim, D. U. Lee, S. S. Shin, J. Seo, E. K. Kim, J. H. Noh and S. I. Seok, *Science*, 2017, **356**, 1376-1379.

[5.18] N. J. Jeon, J. H. Noh, Y. C. Kim, W. S. Yang, S. Ryu and S. I. Seok, *Nature Materials*, 2014, **13**, 897.

[5.19] E. H. Jung, N. J. Jeon, E. Y. Park, C. S. Moon, T. J. Shin, T.-Y. Yang, J. H. Noh and J. Seo, *Nature*, 2019, **567**, 511-515.

[5.20] D. Yang, R. Yang, K. Wang, C. Wu, X. Zhu, J. Feng, X. Ren, G. Fang, S. Priya and S. Liu, *Nature Communications*, 2018, **9**, 3239.

[5.21] J. J. Yoo, S. Wieghold, M. C. Sponseller, M. R. Chua, S. N. Bertram, N. T. P. Hartono, J. S. Tresback, E. C. Hansen, J.-P. Correa-Baena, V. Bulović, T. Buonassisi, S. S. Shin and M. G. Bawendi, *Energy & Environmental Science*, 2019, **12**, 2192-2199.

[5.22] W. Li, H. Dong, L. Wang, N. Li, X. Guo, J. Li and Y. Qiu, *Journal of Materials Chemistry A*, 2014, **2**, 13587-13592.

[5.23] J. Burschka, N. Pellet, S.-J. Moon, R. Humphry-Baker, P. Gao, M. K. Nazeeruddin and M. Grätzel, *Nature*, 2013, **499**, 316.

[5.24] B. Abdollahi Nejand, P. Nazari, S. Gharibzadeh, V. Ahmadi and A. Moshaii, *Chemical Communications*, 2017, **53**, 747-750.

[5.25] Q. Luo, H. Ma, F. Hao, Q. Hou, J. Ren, L. Wu, Z. Yao, Y. Zhou, N. Wang, K. Jiang, H. Lin and Z. Guo, *Advanced Functional Materials*, 2017, **27**, 1703068.

[5.26] P. Docampo, J. M. Ball, M. Darwich, G. E. Eperon and H. J. Snaith, *Nature Communications*, 2013, **4**, 2761.

[5.27] Y. Li, L. Meng, Y. Yang, G. Xu, Z. Hong, Q. Chen, J. You, G. Li, Y. Yang and Y. Li, *Nature Communications*, 2016, **7**, 10214.

[5.28] J. Zhang, H. Luo, W. Xie, X. Lin, X. Hou, J. Zhou, S. Huang, W. Ou-Yang, Z. Sun and X. Chen, *Nanoscale*, 2018, **10**, 5617-5625.

[5.29] J. You, L. Meng, T.-B. Song, T.-F. Guo, Y. Yang, W.-H. Chang, Z. Hong, H. Chen, H. Zhou, Q. Chen, Y. Liu, N. De Marco and Y. Yang, *Nature Nanotechnology*, 2015, **11**, 75.

[5.30] D. Zhao, M. Sexton, H.-Y. Park, G. Baure, J. C. Nino and F. So, *Advanced Energy Materials*, 2015, **5**, 1401855.

[5.31] H. Peng, W. Sun, Y. Li, S. Ye, H. Rao, W. Yan, H. Zhou, Z. Bian and C. Huang, *Nano Research*, 2016, **9**, 2960-2971.

[5.32] W. Chen, Y. Wu, Y. Yue, J. Liu, W. Zhang, X. Yang, H. Chen, E. Bi, I. Ashraful, M. Grätzel and L. Han, *Science*, 2015, **350**, 944-948.

[5.33] J.-Y. Jeng, K.-C. Chen, T.-Y. Chiang, P.-Y. Lin, T.-D. Tsai, Y.-C. Chang, T.-F. Guo, P. Chen, T.-C. Wen and Y.-J. Hsu, *Advanced Materials*, 2014, **26**, 4107-4113.

[5.34] J. R. Manders, S.-W. Tsang, M. J. Hartel, T.-H. Lai, S. Chen, C. M. Amb, J. R. Reynolds and F. So, *Advanced Functional Materials*, 2013, **23**, 2993-3001.

[5.35] J. Zheng, L. Hu, J. S. Yun, M. Zhang, C. F. J. Lau, J. Bing, X. Deng, Q. Ma, Y. Cho, W. Fu, C. Chen, M. A. Green, S. Huang and A. W. Y. Ho-Baillie, *ACS Applied Energy Materials*, 2018, **1**, 561-570.

[5.36] Z. Wu, S. Bai, J. Xiang, Z. Yuan, Y. Yang, W. Cui, X. Gao, Z. Liu, Y. Jin and B. Sun, *Nanoscale*, 2014, **6**, 10505-10510.

[5.37] I. Jung, D. A. Dikin, R. D. Piner and R. S. Ruoff, *Nano Letters*, 2008, **8**, 4283-4287.

[5.38] T. Chen, W. Hu, J. Song, G. H. Guai and C. M. Li, *Advanced Functional Materials*, 2012, **22**, 5245-5250.

[5.39] G. S. Han, Y. H. Song, Y. U. Jin, J.-W. Lee, N.-G. Park, B. K. Kang, J.-K. Lee, I. S. Cho, D. H. Yoon and H. S. Jung, *ACS Applied Materials & Interfaces*, 2015, **7**, 23521-23526.

[5.40] K. Zhang, J. M. Suh, T. H. Lee, J. H. Cha, J.-W. Choi, H. W. Jang, R. S. Varma and M. Shokouhimehr, *Nano Convergence*, 2019, **6**, 6.

[5.41] D.-Y. Lee, S.-I. Na and S.-S. Kim, *Nanoscale*, 2016, **8**, 1513-1522.

[5.42] W. J. d. Silva, A. R. b. M. Yusoff and J. Jang, *IEEE Electron Device Letters*, 2013, **34**, 1566-1568.

[5.43] P. V. Kumar, M. Bernardi and J. C. Grossman, *ACS Nano*, 2013, **7**, 1638-1645.

[5.44] T. Liu, D. Kim, H. Han, A. R. b. Mohd Yusoff and J. Jang, *Nanoscale*, 2015, **7**, 10708-10718.

[5.45] S. Kang, H. Kim and Y.-H. Chung, *Nano Convergence*, 2018, **5**, 13.

[5.46] H. Pan, S. Low, N. Weerasuriya, B. Wang and Y.-S. Shon, *Nano Convergence*, 2019, **6**, 2.

[5.47] E. Jokar, Z. Y. Huang, S. Narra, C.-Y. Wang, V. Kattoor, C.-C. Chung and E. W.-G. Diau, *Advanced Energy Materials*, 2018, **8**, 1701640.

[5.48] E. Stratakis, K. Savva, D. Konios, C. Petridis and E. Kymakis, *Nanoscale*, 2014, **6**, 6925-6931.

[5.49] I. J. Park, M. A. Park, D. H. Kim, G. D. Park, B. J. Kim, H. J. Son, M. J. Ko, D.-K. Lee, T. Park, H. Shin, N.-G. Park, H. S. Jung and J. Y. Kim, *The Journal of Physical Chemistry C*, 2015, **119**, 27285-27290.

[5.50] J. H. Kang, T. Kim, J. Choi, J. Park, Y. S. Kim, M. S. Chang, H. Jung, K. T. Park, S. J. Yang and C. R. Park, *Chemistry of Materials*, 2016, **28**, 756-764.

[5.51] Q.-H. Lu and F. Zheng, in *Advanced Polyimide Materials*, ed. S.-Y. Yang, Elsevier, 2018, DOI: https://doi.org/10.1016/B978-0-12-812640-0.00005-6, pp. 195-255.

Chapter 6. Spiro-OMeTAD/WO_3 Hole Transporting and Buffer Layer for Perovskite Solar Cells with Transparent Electrodes

6.1 Introduction

Many researches are being actively conducted on alternative energy to replace fossil fuels. Solar energy is attracting much attention because it is an infinite energy source and does not cause environmental pollution. In particular, researches on organic-inorganic hybrid perovskite solar cells have increased at a tremendous rate over the last decade. Various properties, such as tunable bandgap energy, high absorption coefficient and long diffusion length, enhance the performances of the devices using perovskite materials. In order to rapidly commercialize perovskite solar cells, research on both the device structure and various layers constituting the solar cell must be conducted along with perovskite, which is a light absorbing material. In order to extend its application into either tandem device with other solar cell or BIPVs or solar panels installed in a field,[6.1] a highly transparent and conductive electrode is required. A sputtered transparent conducting oxide (TCO) is an effective front contact for semi-transparent perovskite solar cells and many TCO materials such as indium tin oxide (ITO), indium zinc oxide (IZO), and aluminum doped zinc oxide (AZO) have been used as transparent electrode. However, these TCO materials are deposited by sputtering process with high energy and requires additional buffer layer to protect the underlying solar cell against

sputtering damage. A hole-selective layer (e.g. MoO_x, WO_3, V_2O_3)[6.2-6.7] or an electron-transporting layer (e.g. ZnO, SnO_2)[6.8] has been used to effectively extract charges and to alleviate the sputtering damage to the underlying perovskite materials. The majority of studies on these bu□er layers have used high cost vacuum-based vacuum processes, such as thermal evaporation,[6.9, 6.10] RF-sputtering,[6.11] and atomic layer deposition (ALD),[6.5] which is incompatible with low cost solution-processed perovskite solar cells. Compared to vacuum process, solution process has benefits such as accessible experimental environment, simple process, and cost advantages. Among the aforementioned metal oxides, WO_3 is an extraordinary sputtering buffer layer for use in perovskite solar cells due to its suitable optical and electrical properties, appropriate work function to perovskite, air stability. Therefore, it is important to research the WO_3 buffer layer fabricated by solution process and demonstrate perovskite solar cell with transparent electrode on the both sides. Even so far, solution processed WO_3 film has not been reported as bu□er layer for sputtered ITO electrode of n-i-p perovskite solar cells.[6.12-6.14]

Herein, we demonstrate that the WO_3 film fabricated by solution process can protect the underlying materials against the sputtering process damage. The WO_3 film with proper thickness and baking temperature exhibits high transparency and appropriate hole transporting properties. Thus, the spiro-OMeTAD/WO_3 hole transporting double layer allow perovskite solar cells to have transparent electrode on the both sides. In addition, the morphology of the WO_3 films can affect the underlying layers and the perovskite performances, thereby resulting in improved diode parameters.

6.2 Properties of WO_3 Film

Figure 6.1(a) shows the transmittance spectra of the WO_3 films on the quartz substrates as a function of thickness with 32, 41, and 54 nm, where the thicknesses were changed by changing the spin-coating speed (Figure 6.2). The WO_3 films are highly transparent in the visible and near-infrared (Vis-NIR) range. The WO_3 film with 32 nm exhibits high transmittance (> 90%) even in 350-400 nm range, and also the WO_3 films with more than 41nm have transmittance enough to pass the light used by perovskite showing better response in the range above 400 nm. The structure of the WO_3 films was investigated by X-ray diffraction (XRD) analysis (Figure 6.1(b)).[6.15] The broad diffraction peak at 15-30 ^{o} indicates that WO_3 films have amorphous structure regardless of the thickness due to the same baking temperature of 120 ^{o}C and are less rigid than crystalline WO_3 with annealing process of high temperature above 330 ^{o}C. In order to demonstrate that the WO_3 film functions as hole transporting layer with spiro-OMeTAD, first the perovskite solar cells were fabricated by introducing WO_3 with various temperatures and thicknesses between the spiro-OMeTAD and Au electrode. Figure 6.3(a) shows current density-voltage ($J-V$) curves of perovskite solar cells as a function of baking temperature of WO_3 films and the solar cell parameters are summarized in Table 6.1. The open-circuit voltage (V_{oc}) and the short-circuit current density (J_{sc}) are barely influenced by the baking temperature except for the reduction of the WO_3 film baked at 140 ^{o}C. The methyl ammonium lead iodide ($MAPbI_3$) perovskite have thermal instability at 120 ^{o}C above and the $MAPbI_3$ perovskite film is decomposed at 140 ^{o}C resulting in

increased shunt resistance (R_{sh}) as observed from the increased slope of $J-V$ curve near J_{sc}.[6.16] Fill factor (FF) increases with the increasing baking temperature, which is a consequence of the reduced series resistance (R_s) as observed from the stiffer slope of $J-V$ curves near V_{oc}. Considering that the boiling point of isopropyl alcohol (IPA) used as solvent is 83 ^oC and the baking time is just 5 min, this reduced R_s can be ascribed to perfect remove of IPA solvent. Figure 6.3(b) and Table 6.2 show the photovoltaic performances of perovskite solar cells as a function of thickness of WO_3 films. The perovskite solar cell was fabricated at the 120 ^oC, which was identified as the optimum temperature. The WO_3 film was used as a buffer layer for damage by the sputtering process, so the thickness was adjusted from thick to thin. The thickness of WO_3 film was made thinner by increasing the speed of spin coating. It can be seen that when the thickness of the WO_3 film are 95 nm and 85 nm, the $J-V$ curves have a low slope near V_{oc}, and thus has a high series resistance. It was shown that the slope of $J-V$ curves increase and the series resistance decrease when the thickness of the WO_3 film is 85 nm or less. The difference in R_s is not large up to about 73 nm, but increases from 46 ohms at 85 nm to 90 ohms at 95 nm. This is because charge transport is not good due to the increased thickness of the WO_3 film.[6.17, 6.18] Thus, it can be seen that R_{sh} decreases due to the recombination of electrons and holes. Therefore, it can be concluded that as the thickness of the WO_3 film decreases, the series resistance of the solar cell decreases. In addition, J_{sc} is low due to low transmittance of the WO_3 film with thickness of 61 nm above as observed from Figure 6.1(a). As a result, the WO_3 film was used by spin-coating with thickness of 54 nm or less and baking at 120 °C in the fabrication of

perovskite solar cells having transparent electrodes on both sides.

Table 6.1 Photovoltaic parameters of the perovskite solar cells as a function of the baking temperature of WO_3 films

Temp. (^oC)	J_{sc} (mA/cm^2)	V_{oc} (V)	Efficiency (%)	FF	Rs ($\Omega\ cm^2$)
80	19.29	0.95	10.43	0.57	78
100	19.58	0.96	12.17	0.65	54
120	19.48	0.98	13.04	0.68	39
140	18.49	0.87	10.11	0.63	35

Table 6.2 Photovoltaic parameters of the perovskite solar cells as a function of the thickness of WO_3 films

Thickness	J_{sc} (mA/cm^2)	V_{oc} (V)	Efficiency (%)	FF	Rs (Ωcm^2) (Ω cm^2)
41 nm	19.96	0.97	13.37	0.69	38
51 nm	19.92	0.97	13.18	0.68	36
54 nm	19.79	0.97	13.32	0.69	34
61 nm	18.99	0.96	12.35	0.68	36
73 nm	18.68	0.96	11.96	0.67	34
85 nm	16.93	0.95	9.16	0.57	46
95 nm	14.51	0.85	5.75	0.47	90

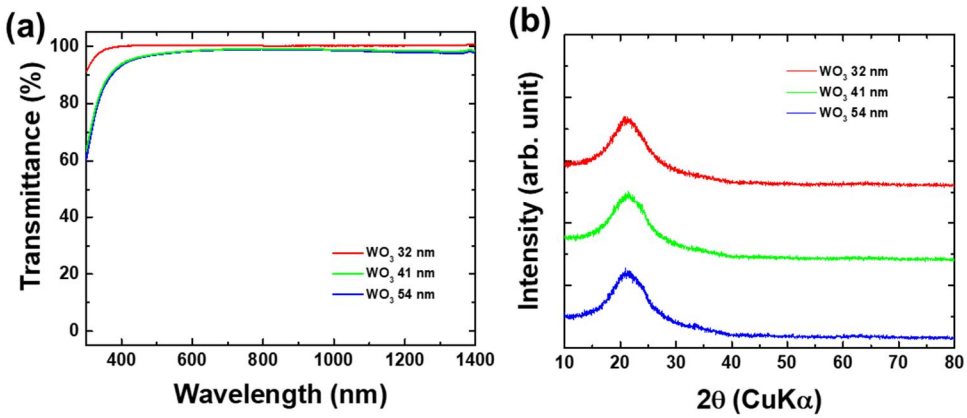

Figure 6.1 Material properties of WO_3 as HTL

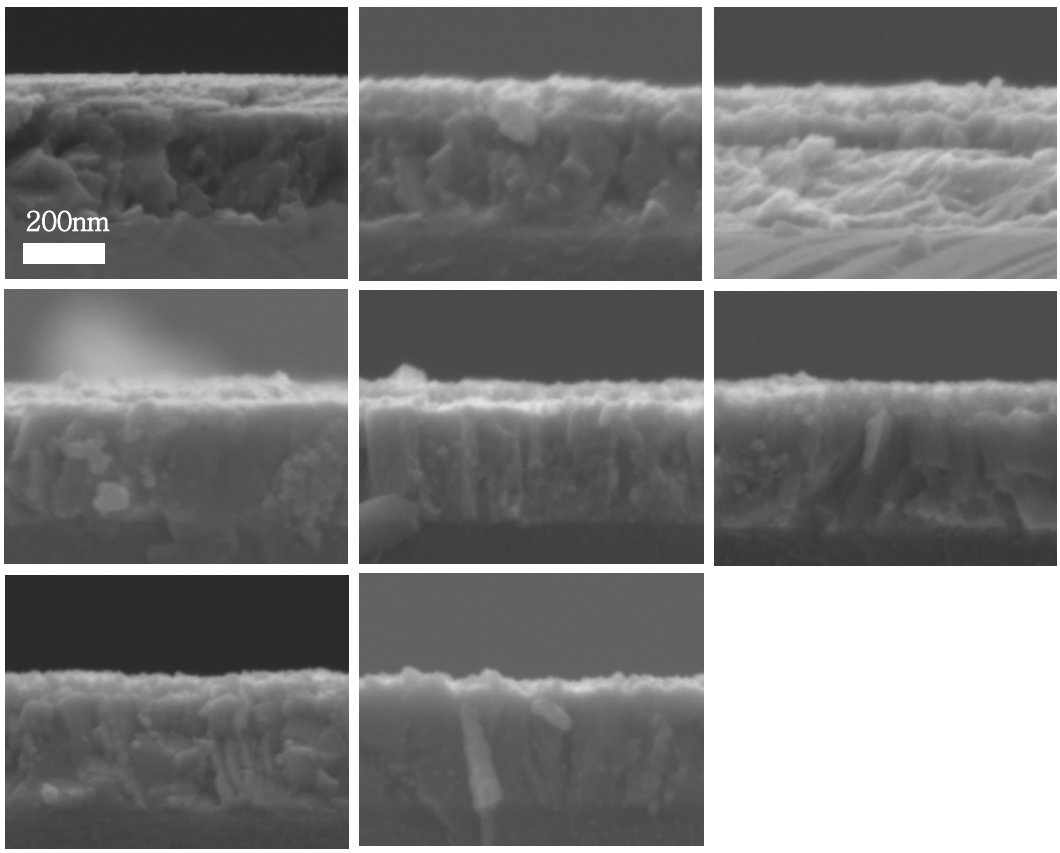

Figure 6.2 Cross sectional FE-SEM images of WO_3 films as a function of the thickness

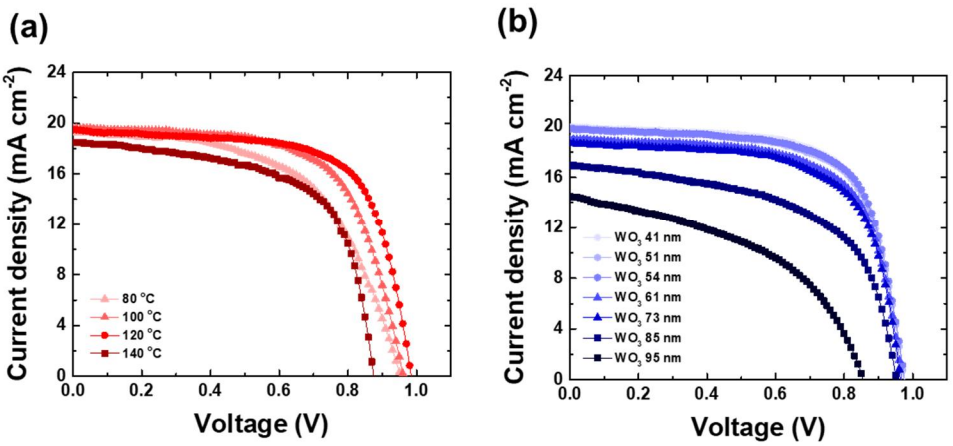

Figure 6.3 *J-V* curves of perovskite solar cells with WO_3 film as a function of fabricating condition.

6.3 Perovskite Solar Cell with transparent electrodes

Figure 6.4(a) and Table 6.3 present the photovoltaic performances of the perovskite solar cells with or without sputtered ITO electrode. The perovskite solar cell without sputtered ITO electrode was fabricated with Au electrode covering the whole active area and the perovskite solar cell shows high photo conversion efficiency (PCE) of 17.59 % with J_{sc} of 23.46 mA cm^{-2}, V_{oc} of 1.03 V, and FF of 0.73. In contrast, the perovskite solar cell with sputtered ITO electrode exhibits deteriorated PCE with J_{sc} of 18.36 mA cm^{-2} and V_{oc} of 0.99 V. In particular, the reduction in FF is noticeable, which can be assumed to be the result of damage of spiro-OMeTAD by the ITO sputtering process. In order to confirm this prediction, an ITO electrode was deposited after spin-coating a WO_3 film on the spiro-OMeTAD layer. Figure 6.4(b) and Table 6.3 present the photovoltaic performances of the perovskite solar cells with sputtered ITO electrode as a function of the thickness of WO_3 films. The perovskite solar cell with Au electrode covering the active area exhibits higher J_{sc} owing to reflecting properties of the Au electrode compared to the solar cells with sputtered ITO electrode. [9] The perovskite solar cells with spiro-OMeTAD/WO_3 double hole transporting layer exhibit decreased V_{oc} compared to the perovskite solar cell with only spiro-OMeTAD, which is ascribed to changed quasi-fermi level due to insertion of WO_3 film and that the V_{oc} of solar cell can be derived from each quasi-fermi levels.[6.19] Figure 6.5(a) shows the photoelectron emission spectra of $MAPbI_3$, spiro-OMeTAD, spiro-OMeTAD/WO_3, and sputtered ITO film on the glass substrates. The work functions (WF) are 5.42 eV and 5.35 eV for spiro-

OMeTAD and spiro-OMeTAD/WO_3, respectively (Figure 6.5(b)). Therefore, increase in WF can influence the change of quasi-fermi level, resulting in reduction of V_{oc} of the perovskite solar cell with a spiro-OMeTAD/WO_3 double hole transporting layer. In particular, the perovskite solar cells with WO_3 films less than 54 nm thick exhibit FF reduced as in the absence of the WO_3 film. Therefore, the diode analysis was conducted to elucidate the reduction of FF observed in the perovskite solar cell with either thin WO_3 films or absence of the WO_3 film.

Figure 6.6(a-c) show the various fitting processes based on the dark J-V curves observed in Figure 6.4(a-b) and the following diode equation.[6.20-6.22]

$$j_{ill} = j_0 \left[exp\left\{ \frac{e(V - jR_S A)}{nkT} \right\} - 1 \right] + \frac{G_{sh}}{A} V - j_{ph}(V) \qquad \text{(Equation 1)}$$

The parallel shunt resistance components and series resistance components should be considered to analyze the diode characteristics of the actual solar cell. The shunt conductance (G_{sh}) and series resistance (R_s) of the solar cells under dark condition can be obtained from the linear fitting of dj/dV and dV/dj values, respectively. The revere saturation current density (j_0) can be obtained from the linear fitting curves calculated from a variation of Equation 1 shown as Figure 6.6(c). All perovskite solar cells show the high R_s except for the perovskite solar cell with only spiro-OMeTAD hole extraction layer without sputtered ITO (*i.e.* spiro (w/o ITO) device) and the perovskite solar cell with spiro-OMeTAD/WO_3 film of 54 nm thickness (*i.e.* spiro/WO_3 54 nm device). The spiro (w/o ITO) device and the spiro/WO_3 54 nm device exhibit the similar value of G_{sh} and J_0 shown as the table 6.4. The G_{sh} and J_0 increase with decreasing thickness of WO_3 films and then the G_{sh} and J_0 display the highest value in the solar cell having sputtered

ITO electrode without WO_3 (*i.e.* spiro). In addition, the S shaped $J-V$ curves shown as Figure 6.4 (a-b) indicate that the perovskite solar cells with thin WO_3 film or without WO_3 film have additional diode caused by the sputtering damage of spiro-OMeTAD.[6.23] Therefore, it can be concluded that the WO_3 film with a thickness of 54 nm or more protects underneath layers during the sputtering process. In order to confirm the protection for spiro-OMeTAD, the electrochemical impedance spectroscopy (EIS) of the devices was conducted in the open-circuit condition of the $J-V$ measurement with the light illumination of the white LED. The recombination kinetics of the solar cells can be analyzed by the imaginary part of the impedance plotted as a function of frequency (Figure 6.7) and the carrier lifetime can be calculated from high-frequency semicircles of the impedance spectrum and the following equation(2):

$$\tau = \frac{1}{\omega_c} = \frac{1}{2\pi f_c} \qquad \text{(Equation 2)}$$

where τ is the lifetime, ω_c is the characteristic radial frequency, and f_c is the characteristic frequency. The carrier lifetime increases with the increasing thickness of WO_3 film, which is a consequence of the tendency for J_0 by diode analysis and ascribed to the protection for spiro-OMeTAD against sputtering damage.

The field emission-scanning electron microscopes (FE-SEM) analysis was performed for further investigating the effects of WO_3 film thickness on the photovoltaic response of the perovskite solar cells with sputtered ITO electrode. Figure 8(a-c) show the surface image of WO_3 films as a function of the thickness. It should be noted that an uncovered area was difficult to observe in cross-sectional image (inserted), but can easily be found in surface images. The uncovered area was calculated by image J program and

plotted as a function of the WO_3 film thickness shown as Figure 6.8(d). The uncovered area decreases with the increasing thickness of WO_3 film, which is consistent with the reduced G_{sh} as summarized in Table 6.4. As a result, the thinner thickness of WO_3 films, the less coverage is achieved, so spiro-OMeTAD suffers from ITO sputtering damage, which reduces the performances of the perovskite solar cells with sputtered ITO electrode.

Figure 6.9 shows the $J-V$ curves of the perovskite solar cell with a sputtered ITO electrode as a function of the illumination direction and the solar cell parameters are summarized in Table 6.5. The J_{sc} are 19.71 mA cm^{-2} and 17.29 mA cm^{-2} under the glass side and sputtered ITO side illumination, respectively. The external quantum efficiency (EQE) was measured over a range from 300 nm to 850 nm for investigating the difference in photo-response of the perovskite solar cells at each wavelength (Figure 6.10). The EQE shows a sharp decrease under wavelength of 400 nm or less and characteristic bends depending on the wavelength. Considering that the WO_3 films exhibit high transparency shown as Figure 6.1(a) and ITO has generally used as transparent conductive electrode in perovskite solar cells, remaining issue is spiro-OMeTAD. Figure 6.11 shows the transmittance spectra of sputtered ITO glass substrates with WO_3 film depending on the presence of spiro-OMeTAD and the transmittance spectra of the substrate with spiro-OMeTAD displays the same shape as EQE. As a result, this difference in the J_{sc} can be ascribed to the parasitic absorption of spiro-OMeTAD. Figure 6.12 shows the transmittance spectra of the perovskite solar cell comprising a the spiro-OMeTAD/WO_3 hole transporting double layer and a sputtered ITO electrode. The transmittance spectrum is remarkably increased in the range above the wavelength

absorbed by the perovskite, and shows a high transmittance of 90% or more, especially at a wavelength of 800-900 nm. Therefore, the perovskite device with sputtered ITO electrode have potential to be used in a variety of applications such as building-integrated photovoltaics (BIPVs), bi-facial solar modules, and tandem solar cells with high efficiency

Table 6.3 Photovoltaic parameters of perovskite solar cell with spiro-OMeTAD/WO_3 HTL double layers.

	J_{sc} (mA/cm^2)	V_{oc} (V)	Efficiency (%)	FF
spiro (w/o ITO)	23.46	1.03	17.59	0.73
spiro	18.36	0.99	7.49	0.41
spiro WO_3 32 nm	21.30	0.93	10.24	0.52
spiro WO_3 41 nm	20.88	0.97	11.87	0.59
spiro WO_3 54 nm	19.71	0.94	12.85	0.69

Table 6.4 Electrical properties of the perovskite solar cell with spiro-OMeTAD/WO_3 HTL double layers and transparent electrodes.

condition	G_{sh} (mS/cm^2)	R_s (Ωcm^2)	A	J_0 (mA/cm^2)
spiro (w/o ITO)	0.00763	0.00437	0.255	2.31245×10^{-9}
spiro	3.91684	0.02672	0.4797	9.20163×10^{-6}
spiro/WO_3 32 nm	0.58785	0.01987	0.4797	1.4513×10^{-6}
spiro/WO_3 41 nm	0.19643	0.03733	0.4797	3.49821×10^{-8}
spiro/WO_3 54 nm	0.009987	0.00791	0.4797	1.38418×10^{-9}

Table 6.5 Photovoltaic parameters of the perovskite solar cell depending on the illumination direction

sample	J_{sc} (mA/cm^2)	Calculated J_{sc} (mA/cm^2)	V_{oc} (V)	Efficiency (%)	FF
glass side	19.71	18.64	0.94	12.85	0.69
ITO side	17.29	14.7	0.96	10.70	0.64

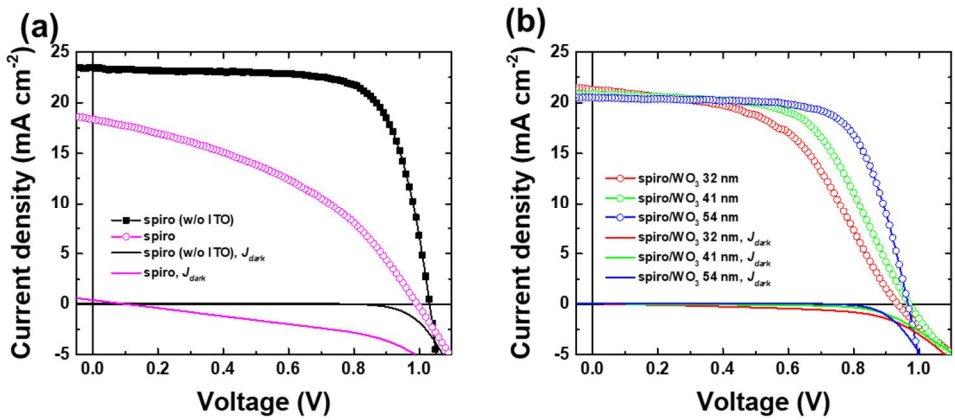

Figure 6.4 *J-V* curves of perovskite solar cells with spiro-OMeTAD/WO_3 HTL double layer and transparent electrode in the both sides

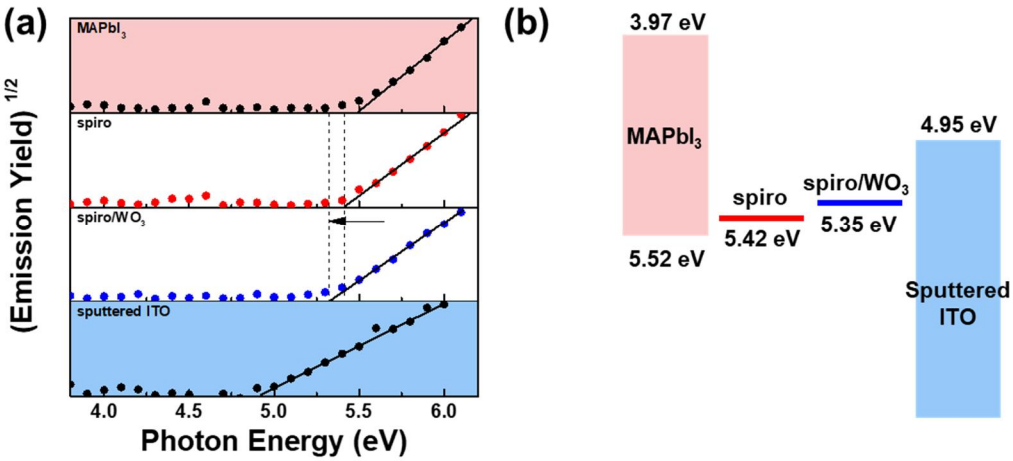

Figure 6.5 The photoelectron emission spectra and energy diagram of HTL and perovskite materials

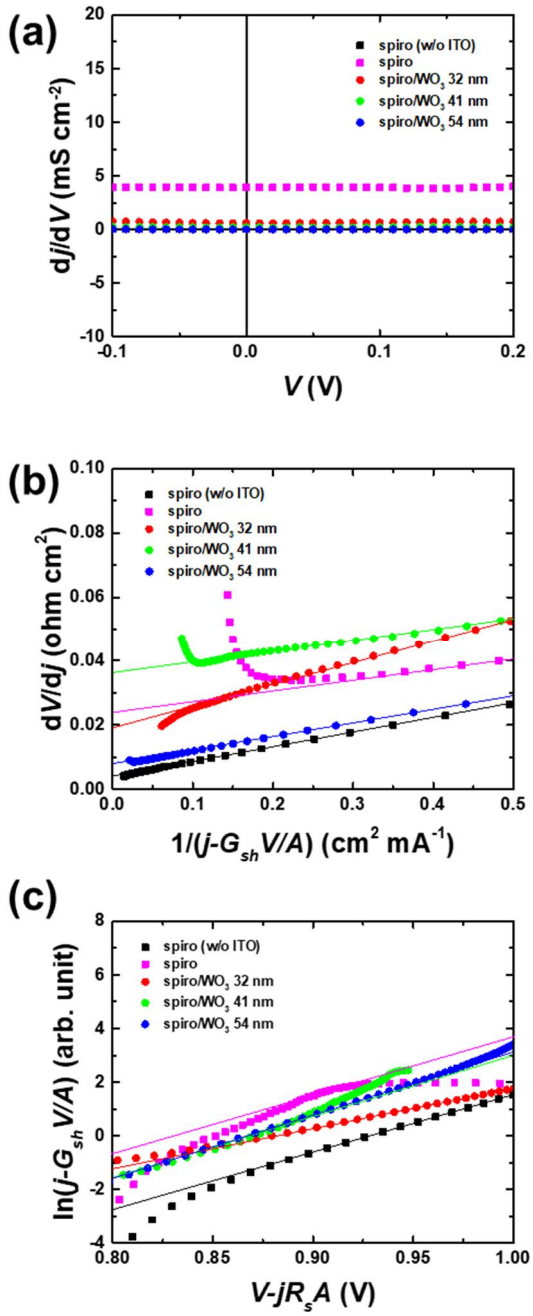

Figure 6.6 Diode characteristics of a) G_{sh} (b) R_s and (c) J_0 of the perovskite solar cells with Spiro-OMeTAD/WO_3 HTL double layer and transparent electrode on the both sides.

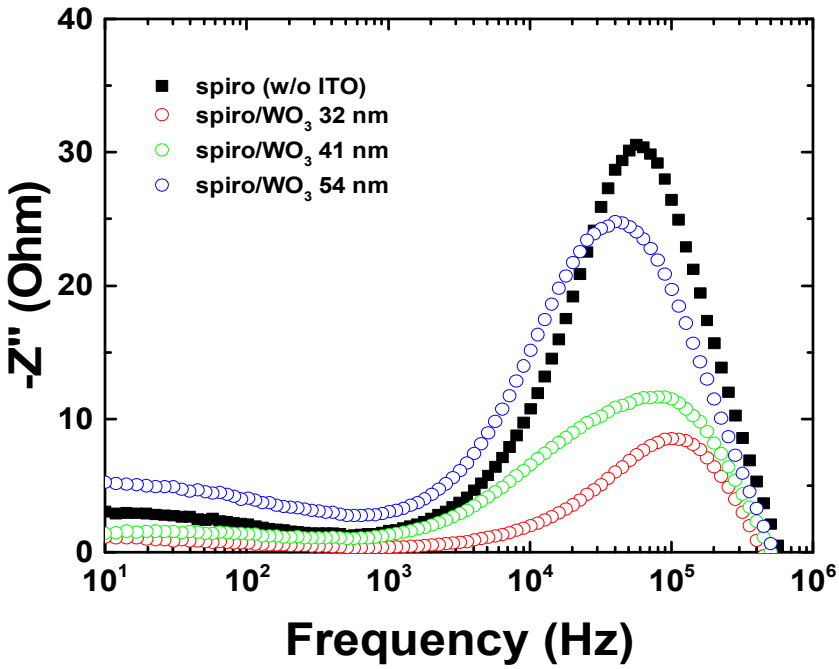

Figure 6.7 Bode plot of perovskite solar cells with spiro-OMeTAD/WO_3 HTL double layer and transparent electrode in the both sides

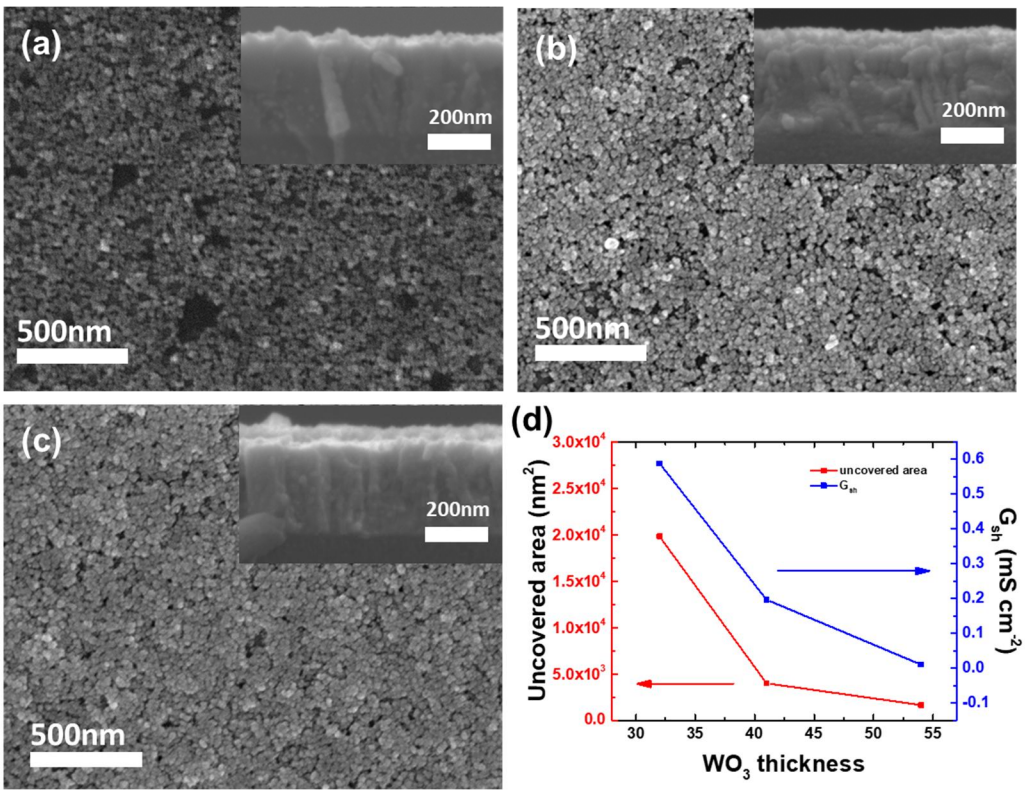

Figure 6.8 The FE-SEM images of the WO_3 films as a function of the thickness

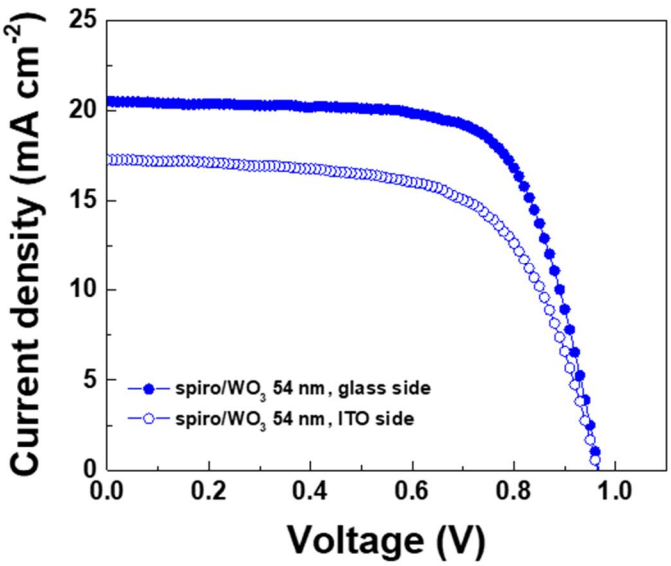

Figure 6.9 *J–V* curves of transparent perovskite solar cells with different directions of light illumination

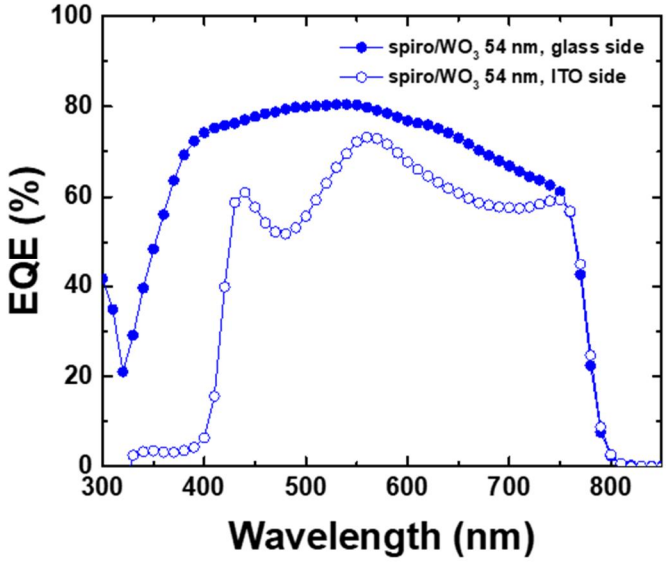

Figure 6.10 EQE curves of the perovskite solar cell with different directions of light illumination

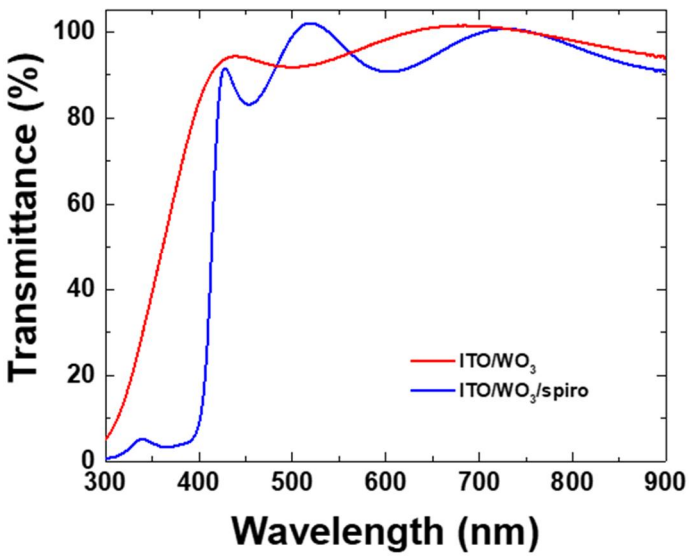

Figure 6.11 Transmittance spectra of glass/ITO/WO_3 layers with and without spiro-OMeTAD.

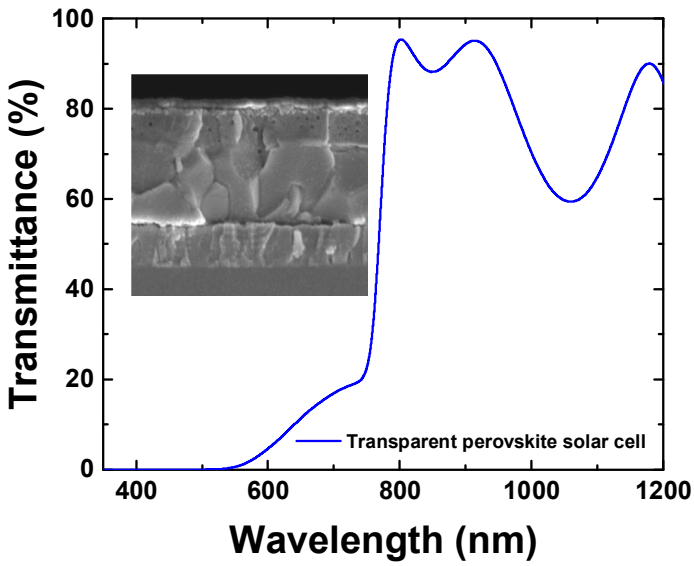

Figure 6.12 Transmittance spectra of perovskite solar cell with transparent electrode in the both sides in the UV-Vis-NIR range.

6.4 Conclusion

In this study, I have successfully demonstrated that the WO_3 film can be used to protect spiro-OMeTAD against ITO sputtering process for the perovskite solar cell with transparent electrode on both sides. In contrast to the perovskite solar cell with only spiro-OMeTAD suffered ITO sputtering damage, the perovskite solar cell with spiro-OMeTAD/WO_3 hole transporting double layer exhibits photo-conversion efficiency of 12.85 %. The WO_3 film with spiro-OMeTAD has played a role as appropriate for hole transporting layer and showed carrier lifetime comparable to only spiro-OMeTAD hole transporting layer. More importantly, it is not necessary to introduce another vacuum process to prevent damage caused by the sputtering process. In conclusion, the introduction of WO_3 film characterized by the facile solution process and low processing temperature below 120 ^{o}C allows the perovskite solar cell to facilitate the application to various devices such as BIPVs, bi-facial solar modules, and tandem solar cells.

6.5 Bibliography

[6.1] Y. Li, J. Duan, Y. Zhao and Q. Tang, Chemical Communications, 2018, 54, 8237-8240.

[6.2] C. Girotto, E. Voroshazi, D. Cheyns, P. Heremans and B. P. Rand, ACS Applied Materials & Interfaces, 2011, 3, 3244-3247.

[6.3] S. Albrecht, M. Saliba, J. P. Correa Baena, F. Lang, L. Kegelmann, M. Mews, L. Steier, A. Abate, J. Rappich, L. Korte, R. Schlatmann, M. K. Nazeeruddin, A. Hagfeldt, M. Grätzel and B. Rech, Energy & Environmental Science, 2016, 9, 81-88.

[6.4] F. Fu, T. Feurer, T. Jäger, E. Avancini, B. Bissig, S. Yoon, S. Buecheler and A. N. Tiwari, Nature Communications, 2015, 6, 8932.

[6.5] J. A. Raiford, R. A. Belisle, K. A. Bush, R. Prasanna, A. F. Palmstrom, M. D. McGehee and S. F. Bent, Sustainable Energy & Fuels, 2019, 3, 1517-1525.

[6.6] C. Lemire, D. B. B. Lollman, A. Al Mohammad, E. Gillet and K. Aguir, Sensors and Actuators B: Chemical, 2002, 84, 43-48.

[6.7] J. Werner, J. Geissbühler, A. Dabirian, S. Nicolay, M. Morales-Masis, S. D. Wolf, B. Niesen and C. Ballif, ACS Applied Materials & Interfaces, 2016, 8, 17260-17267.

[6.8] Y. H. Jang, J. M. Lee, J. W. Seo, I. Kim and D.-K. Lee, Journal of Materials

Chemistry A, 2017, 5, 19439-19446.

[6.9] P. Löper, S.-J. Moon, S. Martín de Nicolas, B. Niesen, M. Ledinsky, S. Nicolay, J. Bailat, J.-H. Yum, S. De Wolf and C. Ballif, Physical Chemistry Chemical Physics, 2015, 17, 1619-1629.

[6.10] J. Werner, G. Dubuis, A. Walter, P. Löper, S.-J. Moon, S. Nicolay, M. Morales-Masis, S. De Wolf, B. Niesen and C. Ballif, Solar Energy Materials and Solar Cells, 2015, 141, 407-413.

[6.11] T. Duong, N. Lal, D. Grant, D. Jacobs, P. Zheng, S. Rahman, H. Shen, M. Stocks, A. Blakers, K. Weber, T. P. White and K. R. Catchpole, IEEE Journal of Photovoltaics, 2016, 6, 679-687.

[6.12] T. Stubhan, N. Li, N. A. Luechinger, S. C. Halim, G. J. Matt and C. J. Brabec, Advanced Energy Materials, 2012, 2, 1433-1438.

[6.13] J. Huang, C. Chou and C. Lin, IEEE Electron Device Letters, 2010, 31, 332-334.

[6.14] J. Arakaki, R. Reyes, M. Horn and W. Estrada, Solar Energy Materials and Solar Cells, 1995, 37, 33-41.

[6.15] S.-J. Wang, M.-C. Wang, S.-F. Chen, Y.-H. Li, T.-S. Shen, H.-Y. Bor and C.-N. Wei, Sensors (Basel), 2018, 18, 2803.

[6.16] E. J. Juarez-Perez, L. K. Ono, M. Maeda, Y. Jiang, Z. Hawash and Y. Qi, Journal of Materials Chemistry A, 2018, 6, 9604-9612.

[6.17] M. Raja, J. Chandrasekaran, M. Balaji and P. Kathirvel, Optik, 2017, 145, 169-180.

[6.18] H. Zheng, J. Z. Ou, M. S. Strano, R. B. Kaner, A. Mitchell and K. Kalantar-zadeh, Advanced Functional Materials, 2011, 21, 2175-2196.

[6.19] S. Ryu, J. H. Noh, N. J. Jeon, Y. Chan Kim, W. S. Yang, J. Seo and S. I. Seok, Energy & Environmental Science, 2014, 7, 2614-2618.

[6.20] J.-O. Jeon, K. D. Lee, L. Seul Oh, S.-W. Seo, D.-K. Lee, H. Kim, J.-h. Jeong, M. J. Ko, B. Kim, H. J. Son and J. Y. Kim, ChemSusChem, 2014, 7, 1073-1077.

[6.21] S. W. Seo, J.-O. Jeon, J. W. Seo, Y. Y. Yu, J.-h. Jeong, D.-K. Lee, H. Kim, M. J. Ko, H. J. Son, H. W. Jang and J. Y. Kim, ChemSusChem, 2016, 9, 439-444.

[6.22] O. Breitenstein, Journal, 2013, 21, 259.

[6.23] H. Kanda, A. Uzum, A. K. Baranwal, T. A. N. Peiris, T. Umeyama, H. Imahori, H. Segawa, T. Miyasaka and S. Ito, The Journal of Physical Chemistry C, 2016, 120, 28441-28447.

Chapter 7. Conclusion

In this thesis, several strategies for stable perovskite solar cells were proposed, which can inspire researchers to solve the current issues of perovskite solar cells for reaching the level of commercialization.

For stability of perovskite solar cells, p–i–n type planar perovskite solar cells incorporating the Li-doped NiO_x hole-extraction layer have been demonstrated, and the influence of the Li doping on the device performance has been investigated. The fill factor of the NiO_x-based perovskite solar cell can be significantly increased by doping Li to NiO_x, while the J_{sc} and V_{oc} are merely influenced. The increased fill factor has been ascribed to the increased electrical conductivity, evidenced by the conductive AFM measurement. It should be noted that the functioning NiO_x layer could be prepared at low temperature of 200 ^{o}C. As a result, the p–i–n type planar perovskite solar cell exhibits an improved conversion efficiency of 15.41% by incorporating the low-temperature Li-doped NiO_x hole extraction layer.

For the flexibility of perovskite solar cells, the GO layer was used for HTL. It has been found out that the GO layer features multiple advantages for the HTL, such as the high transmittance, efficient hole extraction, and good barrier properties. Due to the high transmittance of GO and its appropriate band alignment with the MALI perovskite, conversion efficiencies of 12.31%, 11.39% and 9.34% have been achieved for rigid/non-transparent (glass-substrate/Ag-top), rigid/transparent (glass-substrate/ITO-top), and flexible/transparent (PEN-substrate/ITO-top) perovskite solar cells, respectively. More

importantly, the GO HTL has been found to play a role as a barrier layer for compensating the relatively high water/oxygen permeability of the PEN substrate, resulting in the significantly improved long-term stability (> 120 h) of the flexible/transparent perovskite solar cells. In conclusion, the bi-functional GO layer is a promising HTL for new applications of the perovskite solar cells such as the flexible/wearable solar cells, bi-facial solar cells and the tandem solar cells.

In order to ensure the transparency of the structure, transparent electrodes ware applied to the solar cell of the n-i-p structure. The WO_3 film can be used to protect spiro-OMeTAD against ITO sputtering process for the perovskite solar cell with transparent electrode on both sides. In contrast to the perovskite solar cell with only spiro-OMeTAD suffered ITO sputtering damage, the perovskite solar cell with spiro-OMeTAD/WO_3 hole transporting double layer exhibits photo-conversion efficiency of 12.85 %. The WO_3 film with spiro-OMeTAD has played a role as appropriate for hole transporting layer and showed carrier lifetime comparable to only spiro-OMeTAD hole transporting layer. More importantly, it is not necessary to introduce another vacuum process to prevent damage caused by the sputtering process. In conclusion, the introduction of WO_3 film characterized by the facile solution process and low processing temperature below 120 ^{o}C allows the perovskite solar cell to facilitate the application to various devices such as BIPVs, bi-facial solar modules, and tandem solar cells.

Based on this strategy, perovskite solar cells with stable material-based charge transporting layers have been fabricated, and low temperature solution processing enables application to flexible devices. In addition, the transparent electrodes at both the top and bottom ensure the transparency of the device, thereby improving the possibility

of developing into BIPVs, modules, and tandem solar cells.

Abstract in Korean

국문 초록

유무기 하이브리드 페로브스카이트 물질은 높은 흡광 계수, 긴 캐리어 확산 거리, 낮은 엑시톤 결합 에너지 및 조정 가능한 밴드 갭과 같은 중요한 특성을 갖는다. 이러한 장점으로 인해, 유무기 하이브리드 페로브스카이트 물질은 태양 전지, 발광 다이오드 및 광 검출기와 같은 광전자 분야에서 상당한 관심을 끌었다. 특히, 유무기 하이브리드 페로브스카이트 물질을 광흡수층으로 사용하는 태양 전지는 약 10년의 기간동안 엄청난 속도로 발전하여, 현재 25 % 이상의 높은 광 변환 효율에 도달했다. 그러나, 유무기 하이브리드 페로브스카이트 태양 전지는 안정성, 유연성 및 투명성에 한계가 있어 페로브스카이트 태양 전지의 상용화를 제한한다. 본 논문에서는 이러한 문제를 해결하기 위한 전략들이 제안되었으며, 투명한 전극으로 구성된 페로브스카이트 태양 전지 구조를 통해 다양한 분야로의 적용 및 상용화 가능성이 입증되었다.

먼저, NiO_x 정공전달층과 비교하여 상당히 개선된 충진 계수를 나타내는 Li 도핑 된 NiO_x 정공전달층을 제안하였다. 또한, Li 이온을 도핑함으로써 NiO_x 층의 열처리 온도를 낮출 수 있음이 밝혀졌다. Li 도핑된 NiO_x 정공전달층을 적용한 페로브스카이트 태양전지는 전류 및 광 전압에 변화없이 충

진 계수 향상에 의해 변환 효율이 증가하였다. 전도성 원자력 현미경 연구에 따르면 NiO_x에 Li 이온을 도핑하였을 때, NiO_x 층의 전도성이 크게 증가하여 소자의 직렬 저항이 감소하고 충진 계수와 광전변환 효율이 증가함을 알 수 있었다.

둘째, 다기능성을 띄는 GO층을 페로브스카이트 태양전지의 정공전달층 및 외부환경에 대한 완충층으로 적용하였다. 적절한 두께를 갖는 GO 층은 높은 투과율을 나타내고, 페로브스카이트 층으로부터 효율적으로 정공을 추출하여 페로브스카이트 태양 전지의 우수한 정공수송층으로서 사용될 수 있음을 나타낸다. 특히, GO 층의 장벽 특성은 폴리에틸렌나프탈레이트 (PEN) 기판의 높은 물 / 산소 투과성을 성공적으로 보상하고, 페로브스카이트 태양 전지의 장기 안정성을 상당히 개선시킨다. 또한, 종래의 Ag 상부 전극을 ITO (Indium Tin Oxide) 상부 전극으로 대체하여 투명 페로브스카이트 태양 전지를 제조함으로써, 이중면 광 입사를 가능하게 하여 고효율 탠덤태양전지와 같은 다양한 광전자 소자로의 응용을 가능하게 한다.

마지막으로, n-i-p 구조의 페로브스카이트 태양전지에서도 기존의 spiro-OMeTAD 상부에 WO_3를 용액공정을 통해 증착하여 투명 상부 전극을 적용 가능하게 하였다. 이러한 간단한 공정만으로도 투명전극 형성을 위해 행해지는 스퍼터링 공정의 데미지를 막아 주었고 그 성능에 대한 평가는 소자 특성 평가 및 전기적 특성 평가에 의해 이루어 졌다. 따라서 양방향 입사가 가능한 또 다른 구조의 태양전지를 구현을 통해 기존에 활발히 연구되고

있는 p-i-n 구조의 탠덤태양전지 뿐 아니라 n-i-p 구조의 탠덤태양전지의 구현이 보다 용이 해졌음을 보여준다.

이 논문은 화학적 안정성이 확보된 전하 수송 물질 부족, 유연성이 낮은 소자 구조 및 불투명 전극과 같은 페로브스카이트 태양 전지의 현재 문제에 대한 해결에 중점을 두었다. 안정적인 무기 또는 탄소 기반 정공 수송 물질을 반투명 소자 구조를 가지는 페로브스카이트 태양전지에 적용하여 현재의 문제점을 해결하고 상용화 가능성을 입증하였다. 이러한 연구 결과가 페로브스카이트 태양전지의 상용화 및 다양한 소자로의 활용에 활발하게 적용될 것으로 기대된다.

주요어: 페로브스카이트 태양전지, 전하전달층, 무기기반 전하전달층, 탄소 기반 전하전달층, 소자 안정성, 양방향 조사, 유연 태양전지 소자, 저온 공정

학 번: 2017-33377

Research Achievements

1. List of Publications

1) **M.-A. Park**, I. H. Hong, S. J. Park, S. K. Hwang and J. Y. Kim, Solution processable WO_3 beffer layer for perovskite solar cell with transparent electrode, In preparation.
2) I. H. Hong, † **M.-A. Park**, † and J.Y. Kim, Dye molecule additive engineering for high efficiency perovskite solar cells with long life time and high quality grain, In preparation (†equal contribution)
3) S.J.Sung, † **M.-A. Park**, † J. Park, J.W. Lee, J.Y. Kim and C.R. Park, Transparent all carbon-based electrodes for efficient perovskite solar cells, *Adv. Energy Mater.*, **2019**, submitted. (†equal contribution).
4) **M.-A. Park**, † S.J. Sung, † I.H. Hong, I.J. Park, C.R. Park, and J.Y. Kim, Bi-functional graphene oxide hole-transporting and barrier layers for transparent bi-facial flexible perovskite solar cells, Nanoscale, **2019**, submitted. (†equal contribution)
5) K.B. Cheon, S.K. Hwang, S.W. Seo, J.H. Park, **M.-A. Park** and J. Y. Kim, Roughness-Controlled $Cu_2ZnSn(S,Se)_4$ Thin-Film Solar Cells with Reduced Charge Recombination, ACS Appl. Mater. Interfaces **2019**, 11, 24088-24095.
6) D.S. Lee, S. W. Seo, **M.-A. Park**, K. B. Cheon, S. G. Ji, I. J. Park, J. Y. Kim, Electrochemical approach for preparing conformal methylammonium lead iodide layer on the textured silicon substrate, *Electrochemistry Communications,* **2019**, 103
7) I. J. Park, J.H. Park, S.G. Ji, **M.-A. Park**, J.H. Jang and J. Y. Kim, A Three-Terminal

Monolithic Perovskite/Si Tandem Solar Cell Characterization Platform, Joule 3, 1–12, April 17, **2019**

8) **M .-A. Park**, I.J. Park, S.M. Park, J.H. Kim, W. Jo, H.J. Son, and J.Y. Kim, Enhanced electrical properties of Li-doped NiO_x hole extraction layer, Current Applied Physics, **2018**, 18, S55-S59.

9) I. J. Park**,** G. Kang, **M. A. Park**, J. S. Kim, S. W. Seo, D. H. Kim, K. Zhu, T. Park, J. Y. Kim, Highly efficient and uniform 1 cm^2 perovskite solar cells with an electrochemically deposited NiO_x hole-extraction layer, *ChemSusChem*, **2017**, 202, 48-51.

10) I.J. Park, S. Seo, **M.-A. Park**, S. Lee, D.H. Kim, K. Zhu, H. Shin, and J.Y. Kim, Effect of Rubidium Incorporation on the structural, Electrical, and Photovoltaic Properties of Methylammonium Lead Iodide-Based Perovskite Solar Cells. ACS Appl. Mater. Interfaces **2017**, 9, 41898−41905